

Analysis of Carotid Artery Transverse Sections in Long Ultrasound Video Sequences

Kamil Říha^{a,*}, Martin Zúkal^a, Franz Hlawatsch^{b,a}

^a*Department of Telecommunications, Brno University of Technology,
Brno, Czech Republic*

^b*Institute of Telecommunications, TU Wien, Vienna, Austria*

Abstract

Examination of the common carotid artery (CCA) based on an ultrasound video sequence is an effective method for detecting cardiovascular diseases. Here, we propose a video processing method for the automated geometric analysis of CCA transverse sections. By explicitly compensating the parasitic phenomena of global movement and feature drift, our method enables a reliable and accurate estimation of the movement of the arterial wall based on ultrasound sequences of arbitrary length, and in situations where state-of-the-art methods fail or are very inaccurate. The method uses a modified Viola-Jones detector and the Hough transform to localize the artery in the image. Then, it identifies dominant scatterers aka interest points (IP), whose positions are tracked by means of the pyramidal Lucas-Kanade method. Robustness to global movement and feature drift is achieved by a detection of global movement and subsequent IP re-initialization as well as an adaptive removal and addition of IPs. The performance of the proposed method is

*Corresponding Author: Kamil Říha, Department of Telecommunications, Brno University of Technology, Technická 12, CZ-61600 Brno, Czech Republic.
E-mail: rihak@feec.vutbr.cz, phone: +420541146940

evaluated using simulated and real ultrasound video sequences. Using the Harris detector for IP detection, we obtained an overall root-mean-square error (RMSE)—averaged over all the simulated sequences—of 2.16 ± 1.18 px. The computational complexity of our method is compatible with real-time operation; the runtime is about 30–70 ms/frame for sequences with a spatial resolution of up to 490×490 px. We expect that in future clinical practice, our method will be instrumental for non-invasive early-stage diagnosis of atherosclerosis and other cardiovascular diseases.

Keywords: Artery, ultrasound, image processing, video processing, optical flow, tracking, interest point, Viola-Jones detector, Hough transform, Lucas-Kanade method.

1 **Introduction**

2 *Background and Motivation*

3 As the average age of the global population increases, it is desirable that
4 people with high cardiovascular disease risk be diagnosed and receive ap-
5 propriate treatment. According to WHO statistics, cardiovascular diseases
6 caused 31% of all deaths in the year 2015 (Department of Health Statis-
7 tics and Information Systems, WHO, 2016). Therefore, early detection is
8 an important goal, and this poses challenges for the development of medical
9 devices and diagnostic methods.

10 One of the most important methods for detecting cardiovascular diseases
11 is clinical examination of the *arteria carotis communis*, or common carotid
12 artery (CCA), using an ultrasound (US) video sequence in B-mode. From
13 this video sequence, the movement of the arterial wall can be analyzed as
14 a function of time. This movement depends on diagnostically relevant pa-
15 rameters of the artery such as tissue elasticity (Chen et al., 2009); arterial
16 stiffness (Duprez and Cohn, 2007); compressibility, compliance, or distensi-
17 bility (Gosling and Budge, 2003); and pulse wave velocity (Milnor, 1982).
18 Using a linear probe, the CCA can be scanned in a transverse (perpendic-
19 ular) or longitudinal manner. The longitudinal scan represents the arterial
20 wall as two almost parallel lines, whereas the transverse scan represents it
21 approximately as a circle. Suitable parameters describing the dynamics of
22 these geometric structures are important diagnostic markers.

23 In this paper, we develop and test a non-invasive, fully automated method
24 for the analysis of arterial wall motion. More specifically, we aim to estimate
25 and track the time-varying CCA radius, based on a sequence of CCA trans-

26 verse sections in a US video sequence. The video sequence is captured by a
27 handheld US probe during several minutes. This examination scenario tends
28 to produce two important artifacts, namely, *global movement* and *feature*
29 *drift*. The main goal of our work is to develop strategies and algorithms for
30 compensating global movement and feature drift, in order to enable successful
31 application of our method to examinations *of arbitrary duration*.

32 A global movement arises, e.g., when the examiner searches for the artery
33 position by moving the US probe, which can even cause the artery to move
34 beyond the image border and back during the examination. The feature
35 drift phenomenon is related mainly to micro-movements (shaking) of the
36 probe and/or tissue: the scatterers reflecting the US wave (echogenicity) are
37 randomly appearing and disappearing in the US images, which may lead to
38 errors in tracking the scatterers. Existing methods for a US-based analysis
39 of arterial wall motion (see the next subsection for a survey of the state of
40 the art) are not suited to the analysis of long video sequences because they
41 do not properly take into account the phenomena of global movement and
42 feature drift. The proposed method removes this limitation.

43 *State of the Art*

44 Existing methods for US-based analysis of arterial wall motion typically
45 perform an explicit or implicit tracking of specific scatterers of particular
46 relevance, which are referred to as *interest points* (IPs) or *features*. An IP
47 is a “significant image point” with a high intensity gradient (Harris and
48 Stephens, 1988), which corresponds to a high-echogenicity part of the tissue
49 being scanned and is closely related to *speckle* (Tat et al., 2015). When
50 estimating the motion of the arterial wall from noisy US video sequences, it

51 is advantageous to track elements in successive US images that define the
52 significant structure of the arterial wall. For the choice of such elements,
53 IPs are natural candidates. Accordingly, tracking IPs is a well-established
54 approach to motion analysis in US video sequences.

55 A number of methods for IP-based motion tracking have been proposed.
56 These methods make use of the Lucas-Kanade algorithm (Říha and Potůček,
57 2009), block matching (Golemati et al., 2003; Tat et al., 2015; Thangavel
58 et al., 2014), block matching in combination with a Kalman filter (Gastouni-
59 oti et al., 2010; Zahnd et al., 2013), the “echo tracking” (modified block
60 matching) algorithm (Cinthio et al., 2006, 2005), or a combination of affine
61 optical flow with multiscale image analysis (Gastounioti et al., 2011). Sev-
62 eral methods perform a determination of the *optical flow* (Horn and Schunck,
63 1981), with a preceding manual selection of the region of interest containing
64 the arterial wall. We note that all these methods, with the exception of Říha
65 and Potůček (2009), analyze a longitudinal cut of the artery. A comparison
66 of different optical flow algorithms in (Golemati et al., 2012) obtained the
67 best results with the Lucas-Kanade algorithm, which, however, requires an
68 explicit determination of the IPs prior to optical flow determination. Overall,
69 optical flow algorithms provide good performance in estimating movement in
70 US video sequences corrupted by noise. Therefore, we will use an optical flow
71 algorithm—more specifically, the Lucas-Kanade algorithm—in our method.

72 Optical flow determination can be strongly affected by global movement
73 and feature drift. Current methods for US-based analysis of arterial wall
74 motion do not include a compensation of these detrimental effects. As a
75 consequence, they are able to accurately track the arterial wall only for short

76 US video sequences spanning a small number of cardiac cycles. The proposed
77 method removes this restriction by including an explicit compensation of
78 global movement and feature drift.

79 In addition to tracking IPs, the proposed method also performs an auto-
80 mated estimation of the region containing the arterial wall transverse section
81 and an automated detection of IPs. State-of-the-art methods for estimating
82 the region containing the arterial wall transverse section use pulsative move-
83 ment analysis (Říha and Beneš, 2010), the Viola-Jones algorithm (Říha et al.,
84 2013), circular shape detection (Abolmaesumi et al., 2000), template match-
85 ing (Liu et al., 2013), gradient analysis (Thangavel et al., 2014), an elliptic
86 model of the arterial wall (Wang et al., 2009), or the Star algorithm com-
87 bined with the elliptic model (Guerrero et al., 2007). Methods for explicit IP
88 detection include the Harris detector (Harris and Stephens, 1988), the Good
89 Features to Track (GFTT) method (Shi and Tomasi, 1994), the Features from
90 Accelerated Segment Test (FAST) method (Rosten and Drummond, 2006),
91 scale-space or pyramidal (size-independent) variants of detectors (Lindeberg,
92 1994), and combinations of detectors with feature descriptors, such as Scale
93 Invariant Feature Transform (SIFT) (Lowe, 1999) and Speeded Up Robust
94 Features (SURF) (Bay et al., 2006). These methods were successfully used
95 for US-based analysis of arterial wall motion, as described and referenced at
96 the beginning of this section.

97 *Contributions and Paper Organization*

98 The proposed method is, to the best of our knowledge, the first method
99 allowing an analysis of the movement of the arterial wall based on US video
100 sequences of arbitrary length. It is able to automatically detect, track, and

101 measure the CCA in a transverse-section US video sequence of arbitrary
102 duration. This ability results from a monitoring of global and local CCA pa-
103 rameters, which are used to compensate global movement and feature drift,
104 respectively. The global (macro) parameters of the CCA are the center point
105 and radius of a circle describing the arterial wall cross section. The local (mi-
106 cro) parameters of the CCA are related to IPs that experience feature drift.
107 The proposed compensation of global movement and feature drift based on
108 global and local CCA parameters is a novel approach that enables a highly ro-
109 bust and accurate determination of dynamic CCA parameters independently
110 of the duration of the US video sequence.

111 The remainder of this paper is organized as follows. Next, we present a
112 flowchart of the proposed method and a detailed description of the different
113 steps of the method. Subsequently, we present and discuss experimental
114 results demonstrating the performance and computational complexity of the
115 proposed method.

116 **Method for Analysis of CCA Transverse Sections in Long Video** 117 **Sequences**

118 The input to the proposed method is a sequence of US images (video
119 frames) consisting of transverse scans that were obtained using a linear US
120 probe. The method processes this video sequence in a fully automated way
121 and produces as its output an estimate of the CCA radius as a function of
122 time (frame index t). A flowchart of the method is shown in Fig. 1. The
123 method consists of the following main steps:

124 (i) Estimation of the region containing the arterial wall transverse section;

- 125 (ii) Preliminary estimation of circle parameters (center and radius) describ-
126 ing the arterial wall transverse section;
- 127 (iii) Detection of IPs (see section “State of The Art”) on or near the arterial
128 wall transverse section;
- 129 (iv) Tracking of the IPs over time with compensation of global movement
130 and feature drift;
- 131 (v) Determination of the arterial radius as a function of time.

132 These steps will be discussed in the following subsections.

133 *Region Estimation*

134 As a first step, the proposed method roughly determines the artery posi-
135 tion in the first frame of the US video sequence (frame index $t = 1$). More
136 specifically, the method estimates a square two-dimensional (2D) region of
137 interest in which the arterial wall transverse section is supposed to lie. A
138 standard method for this estimation is the Viola-Jones method (Viola and
139 Jones, 2001). Here, we employ the modified Viola-Jones method presented
140 in Ríha et al. (2013), which improves on the original method through the
141 use of an evolutionary algorithm. Fig. 2 shows an example of the result of
142 artery detection using the modified Viola-Jones detector. More specifically,
143 the figure shows a recorded US image along with a white square indicating
144 the region of interest determined by the detector.

145 *Preliminary Artery Parameter Estimation*

146 In our method, the arterial wall transverse section is modeled by a circle
147 with time-varying center and radius (Golemati et al., 2007; Guerrero et al.,

148 [2007; Liu et al., 2013], which will be briefly referred to as *arterial wall circle*
 149 (AWC). After estimation of the region of interest as discussed above, the
 150 next step is to perform a preliminary estimation of the parameters of the
 151 AWC—center and radius—in the first frame. For this, we use an algorithm
 152 based on the Hough transform ([Duda and Hart, 1972; Golemati et al., 2007]).
 153 The output of the Hough transform is an ordered list of circles, each charac-
 154 terized by its center and radius, where the ordering is according to decreasing
 155 “confidence.” Fig. 3 shows an example of the first ten circles produced by the
 156 Hough transform when applied to a region of interest containing the arterial
 157 wall transverse section.

158 From the list of circles produced by the Hough transform, we determine
 159 preliminary AWC parameters by means of a variant of the procedure de-
 160 scribed in [Říha and Beneš (2010)]. More specifically, the AWC center is cal-
 161 culated as the average of all the centers produced by the Hough transform.
 162 The AWC radius, on the other hand, is derived directly from the image (af-
 163 ter denoising by means of Gaussian blurring and morphological closing, see
 164 [Gonzalez and Woods (2006, ch. 9)]). Let $I(r)$ denote the average intensity of
 165 all those pixels in the denoised image that are intersected by a circle of radius
 166 r about the center point. Then the AWC radius is determined as ([Říha and
 167 Beneš, 2010])

$$\hat{r}_{\text{prel}} = \operatorname{argmax}_{r \in [r_1, r_2]} \left(\frac{\Delta I(r)}{\Delta r} \right), \quad (1)$$

168 where $\Delta I(r)$ represents the difference of two successive discrete values of $I(r)$
 169 and the short notation “ $r \in [r_1, r_2]$ ” expresses the fact that the radius r is
 170 incremented in steps of size Δr from a minimal value r_1 to a maximal value

171 r_2 ; here, Δr corresponds to one pixel.

172 The AWC region/parameter estimation steps described in the previous
173 and present subsections are repeated periodically for global movement detec-
174 tion, as explained in the later subsection titled “Detection and Compensation
175 of Global Movement.”

176 *IP Detection*

177 After AWC region/parameter estimation, IPs are detected and tracked
178 over time. First, an initial set of IPs is detected in the first frame ($t = 1$)
179 of the US video sequence. The initial IPs are searched within an annulus
180 that is defined by the AWC center, the minimum radius $\hat{r}_{\text{prel}} - 1$, and the
181 maximum radius $\hat{r}_{\text{prel}} + w$, where \hat{r} is the preliminary AWC radius as given
182 by (1) and $w > 0$ is a parameter (see Fig. 4). Within this annular search
183 region, IP detection is performed by one of the IP detection methods that
184 were mentioned in the subsection titled “State of the Art.” (An experimen-
185 tal comparison of these methods will be presented later.) The IP detector
186 produces a certain number of IP candidates in the search region. An IP can-
187 didate is accepted if its Euclidean distance to all the IPs accepted thus far is
188 higher than a threshold D_e , and rejected otherwise. This ensures a roughly
189 uniform distribution of IPs within the search region. An example of the total
190 set of accepted IPs is shown in Fig. 5.

191 This IP detection step is repeated under certain conditions, as described
192 in the next subsection.

193 *IP Tracking and Feature Drift Compensation*

194 After an initial set of IPs has been detected as explained above, the IPs
195 are tracked over time: when a new US video frame t becomes available, the
196 set of IPs is updated. This includes a compensation of the feature drift effect.
197 To demonstrate the importance of that compensation, the feature drift effect
198 is illustrated in Fig. 6.

199 The proposed IP tracking method with feature drift compensation per-
200 forms the following three steps: (i) move IPs to new positions; (ii) remove
201 IPs that (after moving) are considered incorrect; (iii) detect new IPs and add
202 them to the IP set. These steps will be discussed in the following. The result
203 of IP tracking including removed and added IPs is visualized in Fig. 7.

204 Step 1: Moving IPs

205 Let $K(t)$ denote the number of IPs at frame time (index) t , and let
206 $\{\mathbf{p}_k(t)\}_{k=1}^{K(t)}$ denote the set of 2D IP coordinates. These coordinates are con-
207 strained to lie on the 2D grid defined by the image pixels. Furthermore, let
208 $I(\mathbf{p}, t)$ denote the image intensity at position $\mathbf{p} = (x, y)$ and frame time t ,
209 and let $I_x(\mathbf{p}, t)$, $I_y(\mathbf{p}, t)$, and $I_t(\mathbf{p}, t)$ denote discrete approximations of the
210 partial derivatives of $I(\mathbf{p}, t)$ with respect to x , y , and t , respectively (Horn
211 and Schunck, 1981). The IP coordinates are moved according to

$$\mathbf{p}_k(t+1) = \mathbf{p}_k(t) + \mathbf{v}_k(t), \quad (2)$$

212 where the velocity vector $\mathbf{v}_k(t)$ is calculated by the pyramidal version (Bouguet,
213 2000) of the Lucas–Kanade (LK) method (Lucas and Kanade, 1981). The
214 LK method determines the velocity $\mathbf{v}_k = (u, v)$ at a given IP position \mathbf{p}_k
215 in a way that is motivated by the optical flow equation (Horn and Schunck,

216 [1981] $I_x(\mathbf{p}_k, t)u + I_y(\mathbf{p}_k, t)v = -I_t(\mathbf{p}_k, t)$. More specifically, the original LK
 217 method minimizes the objective function ([Lucas and Kanade, 1981])

$$f(u, v) = \sum_{i=1}^n (I_x(\mathbf{p}_k^{(i)}, t)u + I_y(\mathbf{p}_k^{(i)}, t)v + I_t(\mathbf{p}_k^{(i)}, t))^2, \quad (3)$$

218 in which $\{\mathbf{p}_k^{(i)}\}_{i=1}^n$ is a set of pixel positions around \mathbf{p}_k where (u, v) can be
 219 considered locally constant. The pyramidal LK method ([Bouguet, 2000]) is a
 220 multiscale version of the original LK method that was observed in [Golemati
 221 et al. (2012)] to provide good results also in the case of fast IP movements
 222 where the original LK method can fail.

223 In some cases, a velocity vector \mathbf{v}_k obtained by the pyramidal LK method
 224 is considered unsuitable, and as a consequence the respective IP k is removed
 225 from the set of IPs (as discussed presently). The criterion for classifying \mathbf{v}_k
 226 as unsuitable is based on the *tracking error* defined as

$$e(k, t) \triangleq \frac{1}{n} \sum_{i=1}^n |I(\mathbf{p}_k^{(i)}, t) - I(\mathbf{p}_k^{(i)} + \mathbf{v}_k, t+1)|. \quad (4)$$

227 Thus, $e(k, t)$ measures the deviation between the intensity values at the local
 228 pixel positions $\mathbf{p}_k^{(i)}$ in the current frame t and the intensity values at the
 229 moved local pixel positions $\mathbf{p}_k^{(i)} + \mathbf{v}_k$ in the next frame $t + 1$.

230 After the IPs have been moved, the AWC is updated to fit the moved
 231 IPs. More specifically, the set of moved IPs is fitted by an ellipse using the
 232 function `fitEllipse` from the OpenCV library ([Bradski, 2000]). Then, the
 233 center of the ellipse is taken as the new AWC center, and the new AWC
 234 radius, \hat{r}_{new} , is calculated from the denoised image according to [1].

235 Step 2: Removing IPs

236 After AWC updating, some of the (moved) IPs are removed from the IP
 237 set. In a first step, we remove all IPs that have an excessive tracking error,
 238 i.e., for which $e(k, t)$ in (4) is larger than a threshold ϵ_e . Then, we remove
 239 those of the remaining IPs that are too distant from the (updated) AWC
 240 in the sense that their Euclidean distances from the AWC center are larger
 241 than $\epsilon_d \hat{r}_{\text{new}}$ or smaller than $\hat{r}_{\text{new}}/\epsilon_d$. Here, ϵ_d is a positive parameter larger
 242 than 1.

243 Step 3: Adding IPs

244 The final step in our IP tracking scheme is to detect new IPs and add
 245 them to the IP set. To this end, we repeat the IP detection procedure
 246 described in the earlier subsection titled “IP Detection,” using an updated
 247 annular search region that is defined by the updated AWC center and radius
 248 discussed above. Those detected IP candidates whose Euclidean distance
 249 to all the existing IPs is higher than our threshold D_e (introduced in the
 250 subsection “IP Detection”) are added to the IP set.

251 Taken together, the three operations discussed above—moving IPs to
 252 new positions, removing “incorrect” IPs, and adding new “correct” IPs—
 253 perform a tracking of IPs with an inherent compensation of feature drift.
 254 This tracking procedure is carried out for each frame t .

255 *Detection and Compensation of Global Movement*

256 In addition to compensating feature drift, the proposed method also de-
 257 tects and compensates global movement in the US video sequence. To this
 258 end, the artery region estimation step and the preliminary artery parameter
 259 estimation step described in our earlier subsections titled “Region Estima-

260 tion” and “Preliminary Artery Parameter Estimation” are repeated every T
 261 frames, where T is a parameter. Each repetition of these steps yields an
 262 AWC, which will be referred to as *reference AWC* in what follows. Based
 263 on the reference AWC, a global movement detection step is then performed.
 264 The result of global movement detection is positive if any one of the following
 265 conditions is satisfied:

- 266 • The distance between the center point of the reference AWC and the
 267 center point of the current AWC (i.e., the updated AWC, cf. our earlier
 268 subsection titled “IP Tracking and Feature Drift Compensation”) is
 269 larger than $\zeta_d \hat{r}$, where \hat{r} is the radius of the current AWC and $\zeta_d > 0$.
- 270 • The radius of the reference AWC is larger than the maximum of the
 271 radii of the current AWC and the past T_r AWCs, multiplied by $\zeta_{r_{\max}} >$
 272 1.
- 273 • The radius of the reference AWC is smaller than the minimum of the
 274 radii of the current AWC and the past T_r AWCs, multiplied by $\zeta_{r_{\min}}$
 275 with $0 < \zeta_{r_{\min}} < 1$.

276 If a global movement is detected, then the current set of IPs is discarded
 277 and a new set of IPs is determined by carrying out the IP detection step
 278 described in our earlier subsection titled “IP Detection.”

279 *Estimation of AWC Radius*

280 The result of the proposed analysis method is an estimate $\hat{r}(t)$ of the
 281 AWC radius $r(t)$ as a function of the frame index t . This estimate is derived
 282 for each t from the IP set resulting from the IP tracking step explained in

283 our earlier subsection titled “IP Tracking and Feature Drift Compensation.”
284 More specifically, an ellipse is fitted to that IP set by means of the function
285 `fitEllipse` from the OpenCV library (Bradski, 2000). Then, $\hat{r}(t)$ is taken
286 to be the average of the semi-major and semi-minor axes of the ellipse.

287 **Results and Discussion**

288 In this section, we present experimental results demonstrating the per-
289 formance and computational complexity of the proposed method and, in
290 particular, its robustness to global movement, speckle noise, additive noise,
291 and feature drift.

292 *Patients and Acquisition Hardware*

293 The data involved in the following experiments were mostly created by dif-
294 ferent simulation procedures. As an input of those simulation procedures, we
295 used two US measurements taken on two different human subjects, namely, a
296 healthy test subject aged 32 years and a diseased test subject aged 72 years.
297 These measurements were performed with the subjects’ informed consent and
298 with approval of the ethics committee. The hardware used for this acqui-
299 sition was an Ultrasonix OP device with linear probe L145/38 (Ultrasonix
300 Medical, Richmond, BC, Canada).

301 *Basic Experimental Setup*

302 For each of the four phenomena mentioned above—i.e., global movement,
303 speckle noise, additive noise, and feature drift—we created a corresponding
304 “ground-truth” video sequence with known time-varying position and size
305 of the CCA transverse section. These ground-truth video sequences allow

306 a quantitative evaluation of the accuracy of the CCA analysis in video se-
307 quences of arbitrary length. Their creation was based on a motion model
308 that will be described in the next subsection.

309 We compare the proposed method with a variant of the method in which
310 the compensation of feature drift and global movement is omitted, as is
311 common in current methods. This variant will be referred to as “reference
312 method.” In both the proposed method and the reference method, the pyra-
313 midal LK method is used for IP tracking. However, the reference method
314 does not include the steps of removing and adding IPs. Within both methods,
315 we use and compare the following eight alternative IP detectors, which were
316 mentioned and referenced in the subsection titled “State of the Art”: FAST,
317 GFTT, Harris, pyramidal FAST (abbreviated Pyr-FAST), pyramidal GFTT
318 (Pyr-GFTT), pyramidal Harris (Pyr-Harris), SIFT, and SURF. The specific
319 values of Hough transform parameters that we used in our experiments (cf.
320 the subsection “Preliminary Artery Parameter Estimation”) are as follows:
321 resolution of the Hough space field = 1 px, minimal distance between the cen-
322 ters of detected circles = 1 px, threshold for circle center detection = 30, min-
323 imal circle radius $r_1 = 20$ px, and maximal circle radius $r_2 = 80$ px. Further
324 parameter values used in the simulations—introduced earlier—are $w = 4$ px
325 (except for SIFT and SURF), $t = 120$, $D_e = 4$ px, $\epsilon_e = 30$, $\epsilon_d = 1.1$ (except
326 for SIFT and SURF), $\zeta_d = 0.5$, $t_r = 1500$, $\zeta_{r_{\max}} = 1.1$, and $\zeta_{r_{\min}} = 0.91$. The
327 SIFT and SURF algorithms for IP detection use different values of w and ϵ_d
328 because they need a larger neighborhood for detecting a sufficient number of
329 IPs: for SIFT, $w = 12$ px and $\epsilon_d = 1.2$, and for SURF: $w = 16$ px and $\epsilon_d = 1.2$.

330 For quantifying the accuracy of the various methods, we use the root mean

331 square error (RMSE) between a “ground-truth” AWC radius $r_0(t)$ and the
 332 estimated radius $\hat{r}(t)$, averaged over the total number of processed frames,
 333 M , i.e.,

$$\text{RMSE} = \sqrt{\frac{1}{M} \sum_{t=1}^M (\hat{r}(t) - r_0(t))^2}. \quad (5)$$

334 *Motion Model*

335 The definition of the ground-truth radius function $r_0(t)$ was based on a
 336 model of the time-varying AWC radius $r(t)$. For this model, we adopt the
 337 radial part of the motion model described in [Stoitsis et al. \(2008\)](#). This
 338 is based on the assumption that the artery can be well approximated by a
 339 circle ([Golemati et al., 2007](#); [Guerrero et al., 2007](#); [Liu et al., 2013](#))—i.e., the
 340 AWC—, that the arterial wall is isotropic, and that the pulsative changes
 341 related to the blood pressure changes are isovolumetric ([Gosling and Budge,](#)
 342 [2003](#)).

343 The radial part of the motion model in [Stoitsis et al. \(2008\)](#) involves cer-
 344 tain parameters, hereafter referred to as “motion model parameters.” Sim-
 345 ilarly to [Stoitsis et al. \(2007\)](#), we determined these parameters by fitting
 346 them to one cardiac cycle of an estimated AWC radius function $\hat{r}_{\text{ref}}(t)$. The
 347 function $\hat{r}_{\text{ref}}(t)$ is shown in Fig. 8a; it was estimated by the reference method
 348 from a real US video sequence. This sequence was acquired in vivo as de-
 349 scribed in section “Patients”. One can see in Fig. 8a that $\hat{r}_{\text{ref}}(t)$ comprises
 350 approximately 30 cardiac cycles and includes breathing artifacts, which are
 351 visible as a low-frequency component. We selected one cardiac cycle and
 352 expressed the corresponding values of $\hat{r}_{\text{ref}}(t)$ as a normalized displacement
 353 $\hat{d}_{\text{ref}}(t)$ relative to the diastolic radius, i.e., the diastolic radius was subtracted

354 and the result was divided by the maximal (systolic) radius. The function
355 $\hat{d}_{\text{ref}}(t)$, shown in Fig. 8b, constituted the input to the fitting procedure de-
356 scribed in [Coleman and Li \(1996\)](#), which produced the fitted (based on the
357 underlying model) displacement function $d(t)$ shown in Fig. 9a. It can be
358 seen that both $\hat{d}_{\text{ref}}(t)$ and $d(t)$ conform to the typical pulse wave shape: they
359 start from, and end in, zero (diastolic) displacement, and they assume their
360 maximum in the systole, which is followed by the dicrotic notch.

361 The fitting procedure described in [Coleman and Li \(1996\)](#) also provided
362 the motion model parameters corresponding to $d(t)$. These parameters were
363 as follows: $t_1 = 7.2932$, $t_2 = 7.2502$, $a = 2.2738$ mm, $b = -1 \cdot 10^{-5}$, $c = 0.0215$,
364 $d = 0.1157$, and $T_p = 22$ frames. These parameters were used in all the
365 simulations reported below except those exploring the robustness to feature
366 drift.

367 The function $d(t)$ described above does not include breathing artifacts. To
368 include this low-frequency phenomenon in our motion model, we constructed
369 a periodic function consisting of 22 repetitions of $d(t)$ and added to it a
370 sinusoidal function as described in [Schlaikjer et al. \(1998\)](#). The corresponding
371 radius function $r_0(t)$, which is shown in Fig. 9b, was used as “ground-truth”
372 AWC radius function in all simulations except those exploring the robustness
373 to feature drift.

374 *Results for an Uncorrupted Sequence*

375 In this and the next four subsections, we present experimental results
376 for a variety of different scenarios. First, we consider an idealized, simu-
377 lated “ground-truth” video sequence without any corruptions such as global
378 movement, noise, or feature drift. This sequence, hereafter denoted as S_0 ,

379 was created by using a real (measured) US image as the first video frame
380 and generating the subsequent frames through geometric deformations. The
381 measured image, which is shown in Fig. 10, was extracted from the real US
382 video sequence mentioned in the previous subsection at the end of the dias-
383 tole of the first cardiac cycle. The spatial resolution of the image is 370×370
384 px. The geometric deformations producing the subsequent frames were per-
385 formed as follows. First, the position of the artery center in the image and
386 the artery radius were defined manually. Then, for each frame t of S_0 , the
387 measured image was locally transformed such that the artery radius equaled
388 the “ground-truth” AWC radius $r_0(t)$. More specifically, the pixels located
389 at the AWC were translated in the radial direction over a distance defined
390 by $r_0(t)$, and the pixels located near the AWC were translated in a similar
391 manner but over a distance that decreases with a larger distance from the
392 AWC, as described in [Stoitsis et al. \(2008\)](#). This local image transformation
393 was performed using the function `remap` (with bilinear interpolation) from
394 the OpenCV library ([Bradski, 2000](#)).

395 Table 1 shows the RMSE results obtained for the sequence S_0 by the
396 proposed method and by the reference method using the eight alternative
397 IP detectors. One can see that here, i.e., in the absence of any corruptions,
398 the proposed method typically does not outperform the reference method.
399 In fact, for two of the eight IP detectors—SIFT and SURF—the RMSE is
400 even significantly larger. This is because in the absence of feature drift, the
401 feature drift compensation performed by the proposed method may produce
402 additional IP tracking errors.

403 *Robustness to Global Movements*

404 To evaluate the performance of the proposed method and the reference
 405 method in the presence of global movement, we created a video sequence S_P
 406 by applying a frame-dependent horizontal translation to each frame of the
 407 uncorrupted sequence S_0 , with symmetric repetition of the pixels in the areas
 408 that needed to be filled after the translation. The effect of this translation
 409 was to move the pulsating AWC out of the visible area of the image and back.
 410 Four frames from S_P are shown in Fig. 11. The RMSE results obtained for S_P
 411 are provided in Table 2. One can see that the proposed method significantly
 412 outperforms the reference method: irrespective of the IP detector used, the
 413 reference method effectively fails whereas the results of the proposed method
 414 are still reasonably accurate.

415 *Robustness to Speckle Noise*

416 To evaluate the performance of the two methods in the presence of speckle
 417 (multiplicative) noise, we created a noisy video sequence as

$$f_t(\mathbf{x}) = g_t(\mathbf{x})(1 + u_t(\mathbf{x})), \quad (6)$$

418 where $g_t(\mathbf{x})$ is the t th frame in the uncorrupted sequence S_0 and $u_t(\mathbf{x})$ is 2D
 419 noise that is zero-mean, uniformly distributed, and independent and identi-
 420 cally distributed (iid) across the pixels — i.e, \mathbf{x} — and across t . The variance
 421 of $u_t(\mathbf{x})$ was chosen such that a signal-to-noise ratio (SNR) of 25 dB or 15 dB
 422 was obtained for each frame t . That is,

$$\sigma_{u_t}^2 = \frac{\sigma_{g_t}^2}{10^{\text{SNR}[\text{dB}]/10}}, \quad (7)$$

423 where $\sigma_{g_t}^2$ is the empirical variance of $g_t(\mathbf{x})$, which was determined by aver-
 424 aging over all pixels \mathbf{x} in frame t , and $\text{SNR}[\text{dB}] = 25$ or 15 . The resulting
 425 sequences are denoted as S_{S25} and S_{S15} , respectively. Example images from
 426 these sequences are shown in Fig. 12.

427 The RMSE results for S_{S25} and S_{S15} are provided in Table 3. It can be seen
 428 that for almost all IP detectors, and most notably for the low-SNR sequence
 429 S_{S15} , the proposed method is significantly more robust to speckle noise than
 430 the reference method. This robustness is due to the fact that multiplicative
 431 speckle noise effectively causes feature drift, which is compensated by the
 432 proposed method. For the low-SNR sequence S_{S15} , some of the RMSE values
 433 in Table 3 are very high. One can conclude that, at least for some part of
 434 the sequence, some of the tracked IPs are far away from the arterial wall or,
 435 in other words, the artery is temporarily lost during the tracking procedure.
 436 This effect is much more pronounced for the reference method than for the
 437 proposed method, for almost all of the eight IP detectors. However, one
 438 case of lost artery occurred also with the proposed method using the FAST
 439 detector.

440 *Robustness to Additive Noise*

441 To analyze the performance in additive noise, we created a sequence of
 442 noisy images

$$f_t(\mathbf{x}) = \mathcal{C}\{g_t(\mathbf{x}) + \eta_t(\mathbf{x})\}, \quad (8)$$

443 where $g_t(\mathbf{x})$ is again the t th frame in the uncorrupted sequence S_0 , $\eta_t(\mathbf{x})$ is
 444 2D Gaussian noise that is iid across the pixels and across t , and $\mathcal{C}\{\cdot\}$ is a
 445 clipping operation that restricts the intensity to the displayable range. The

446 mean of $\eta_t(\mathbf{x})$ was chosen equal to the empirical mean of $g_t(\mathbf{x})$ averaged
447 over all pixels \mathbf{x} in frame t . The variance of $\eta_t(\mathbf{x})$ was chosen such that an
448 SNR (before clipping) of 25 dB or 15 dB was obtained for each frame t . The
449 resulting sequences are denoted S_{G25} and S_{G15} , respectively; example images
450 are shown in Fig. 13.

451 The RMSE results provided in Table 4 show that, with one exception
452 (PyR-FAST detector for sequence S_{G15}), the proposed method is slightly less
453 robust to additive Gaussian noise than the reference method. We can con-
454 clude that additive Gaussian noise causes the proposed compensation of fea-
455 ture drift and global movement to produce small additional errors. This effect
456 is inverse to the effect of speckle noise studied in the previous subsection,
457 where the proposed method was seen to exhibit superior robustness. How-
458 ever, a comparison of the RMSE results in Table 4 with the RMSE results
459 obtained in the sections “Robustness to global movement”, “Robustness to
460 speckle noise”, and “Robustness to feature drift” (see below) shows that the
461 deterioration in the case of additive Gaussian noise is typically much weaker
462 than the improvements obtained in the presence of global movement and/or
463 significant speckle noise and/or significant feature drift.

464 *Robustness to Feature Drift*

465 Feature drift is caused by a fluctuation of echogenicity, which is due to
466 small relative movements between the US probe and the tissue in the di-
467 rection perpendicular to the image plane. To simulate this situation, we
468 created three video sequences by means of the US simulation program Field
469 II (Jensen, 1997), which allows the simulation of US systems and US imaging
470 using linear acoustics.

471 More specifically, using suitable Field II routines, we performed a simula-
 472 tion in which a virtual US probe captures a virtual object that is represented
 473 by scatterers spread in a phantom. Motivated by the procedure described in
 474 [Jensen and Munk \(1997\)](#), we created 100000 randomly spread scatterers in
 475 a phantom defined by a cuboid of base area 60×60 mm (which lies in the
 476 image plane) and height 10 mm (in the direction perpendicular to the image
 477 plane). The scatterer amplitudes were chosen between 0 and 167 according
 478 to the manually created echogenicity (intensity) map shown in Fig. 14, which
 479 is intended to approximate the real US image in Fig. 10. Furthermore, we
 480 defined the characteristics of a virtual linear US probe (transducer) in the
 481 Field II simulation ([Jensen, 1997](#)) according to the following parameters: cen-
 482 ter frequency of transducer $f_0 = 5$ MHz, sampling frequency $f_s = 100$ MHz,
 483 speed of sound $c = 1540$ m/s, wavelength (width of a transducer element)
 484 $\lambda = 0.308$ mm, element height $h = 5$ mm, distance between transducer el-
 485 ements (*kerf*) = 0.05 mm, number of transducer elements $N_e = 192$, and
 486 number of active transducer elements $N_a = 64$. The choice of these pa-
 487 rameter values was inspired by the physical probe mentioned in the section
 488 “Patients and Acquisition Hardware.” An image created by means of this
 489 simulation procedure is shown in Fig. 15; the spatial resolution is 490×490
 490 px.

491 Next, we created a video sequence, denoted S_{F0} , in a similar manner as
 492 the sequence S_0 (cf. the earlier subsection titled “Results for an Uncorrupted
 493 Sequence”) except for the following two differences: (i) the first image of
 494 S_{F0} is the simulated image shown in Fig. 15, instead of the measured US
 495 image shown in Fig. 10, and (ii) the parameters a and b of the motion model

496 used to generate the AWC radius $r(t)$ were chosen as $a = 0.4\text{mm}$ and $b =$
497 -0.1722 . We note that this choice of a and b conforms to the choice in
498 [Stoitsis et al. \(2008\)](#), whereas that in all the remaining simulations in our
499 study was motivated by the real measurement data used to create S_0 .

500 Finally, we converted the sequence S_{F_0} into two sequences S_{F_2} and S_{F_5}
501 simulating the micro-movement of scatterers. This was done by replacing, in
502 each image of S_{F_0} , 2% or equivalently 2000 randomly selected scatterers (for
503 S_{F_2}) or 5% or equivalently 5000 randomly selected scatterers (for S_{F_5}) with
504 the same number of new scatterers. The positions of the new scatterers were
505 randomly chosen in a circular neighbourhood of radius 1 mm (corresponding
506 to approximately 8 px) around the respective replaced scatterer, and their
507 amplitudes were randomly chosen within a range from one tenth to ten times
508 the amplitude of the respective replaced scatterer.

509 The RMSE results for the sequences S_{F_2} and S_{F_5} are reported in Table 5.
510 One can see that the robustness to feature drift of the proposed method is
511 similar to that of the reference method for S_{F_2} but significantly better for
512 S_{F_5} . This shows the effectiveness of the proposed feature drift compensation.

513 *Overall RMSE Results*

514 With the goal of identifying the best IP detector, we determined the total
515 RMSE averaged over all the test sequences— S_0 , S_P , $S_{S_{25}}$, $S_{S_{15}}$, $S_{G_{25}}$, $S_{G_{15}}$,
516 S_{F_0} , S_{F_2} , and S_{F_5} —for the proposed method and for the reference method us-
517 ing the various IP detectors. These total RMSE results are shown in Table 6
518 in the form $\mu \pm \sigma$, where μ is the average taken over the nine test sequences
519 and σ is the corresponding standard deviation. One can see that, on average,
520 the proposed method significantly outperforms the reference method, except

521 when FAST is used as IP detector. The proposed method performs best
522 when the Harris detector is used, closely followed by the GFTT detector.

523 *Computational Complexity*

524 Finally, we report the runtimes of a C++ implementation of the pro-
525 posed method on a PC with quad-core processor Intel Core i5-2320 (clock
526 frequency 3.00 GHz) and 16 GB RAM. The operating system was 64-bit
527 Windows 7 SP 1. Our C++ program used certain routines of the OpenCV
528 library. Tables 7 and 8 consider the sequences S_0 , S_P , S_{S25} , S_{S15} , S_{G25} , and
529 S_{G15} , which have an image resolution of 370×370 px. The tables list the
530 runtimes of four different parts of the proposed method: Table 7 considers
531 artery region/parameter estimation (see Sections “Region Estimation” and
532 “Preliminary Artery Parameter Estimation”) and IP tracking with feature
533 drift compensation (see Section “IP Tracking and Feature Drift Compensa-
534 tion”), and Table 8 considers IP detection using the various IP detection
535 methods (see Section “IP Detection”). The runtimes are given in the form
536 $\mu \pm \sigma$, where μ is an average and σ is a standard deviation. Tables 9 and
537 10 report the runtimes for the sequences S_{F0} , S_{F2} , and S_{F5} , which have an
538 image resolution of 490×490 px.

539 According to Tables 7–10, the most complex part of the proposed method
540 is the artery region/parameter estimation step. This is primarily caused by
541 the Viola-Jones algorithm used for artery region estimation. Within our
542 implementation, the runtime of this part is several tens of milliseconds.
543 The runtimes of the remaining parts—IP detection, IP tracking, and fea-
544 ture drift compensation—are only a few milliseconds (except IP detection
545 using SIFT). However, the artery region/parameter estimation part is only

546 performed at the beginning and then every $T = 120$ frames. In practice, the
547 frame rate of US records is typically 30–50 frames per second, corresponding
548 to a frame duration of 20–30 ms. This means that our implementation of
549 the proposed method is almost compatible with real-time operation. Full
550 real-time operation—at the cost of some reduction of the accuracy of artery
551 radius estimation—can be obtained by skipping the processing of frames
552 while completing an artery region/parameter estimation step.

553 *Performance for Real Data*

554 In Fig. 16, we show results of our method for real clinical data. The data
555 were acquired on a healthy 32-year-old subject (Fig. 16a) and on a 72-year-
556 old subject with atherosclerosis (Fig. 16b). One can see that for the diseased
557 subject, the radius curve estimated by our method has a smaller amplitude
558 and is more noisy than for the healthy subject. This fact may be diagnosti-
559 cally significant for non-invasive early-stage detection of atherosclerosis.

560 **Conclusion**

561 We have proposed a method enabling the dynamic analysis of an artery
562 transverse section based on an ultrasound video sequence of arbitrary length.
563 A distinctive new feature and major advantage of the proposed method are
564 its inherent robustness to the parasitic phenomena of global movement and
565 feature drift. Because the effects of global movement and feature drift are
566 compensated, the proposed method yields reliable operation and accurate
567 radius estimates for ultrasound video sequences of arbitrary length and in
568 situations where state-of-the-art methods fail or are very inaccurate, includ-
569 ing the case where the artery is moved out of and back into the image field.

570 The best performance was achieved using the Harris detector for interest
571 point detection. The computational complexity of the proposed method is
572 compatible with real-time operation. We conjecture that in future clinical
573 practice, our method has a high potential for automated non-invasive deter-
574 mination of dynamic parameters related to artery tissue elasticity (stiffness,
575 compressibility, compliance, etc.) and, in turn, for early-stage detection of
576 atherosclerosis and other cardiovascular diseases.

577 **Acknowledgements**

578 This work was supported in part by the Czech Science Foundation (GACR)
579 under Grant 17-19638S, by the Austrian Science Fund (FWF) under Grant
580 P27370-N30, and by the European Research Council within the National Sus-
581 tainability Programme of the European Commission under Grant LO1401.

582 **References**

- 583 Abolmaesumi P, Sirouspour MR, Salcudean SE. Real-time extraction of
584 carotid artery contours from ultrasound images. In: Proc. 13th IEEE Sym-
585 posium on Computer-Based Medical Systems. Houston, TX, USA, 2000.
586 pp. 1063–7125.
- 587 Bay H, Tuytelaars T, Gool LV. SURF: Speeded up robust features. In: Proc.
588 9th European Conference on Computer Vision (ECCV'06). Graz, Austria,
589 2006. pp. 404–417.
- 590 Bouguet JY. Pyramidal Implementation of the Lucas Kanade Feature
591 Tracker: Description of the Algorithm. Tech. rep., Intel Corporation Mi-
592 croprocessor Research Labs, 2000.
- 593 Bradski G. The OpenCV library. Dr. Dobb's Journal of Software Tools,
594 2000;25:120–126.
- 595 Chen L, Treece GM, Lindop JE, Gee AH, Prager RW. A quality-guided
596 displacement tracking algorithm for ultrasonic elasticity imaging. Medical
597 Image Analysis, 2009;13:286–296.
- 598 Cinthio M, Ahlgren ÅR, Bergkvist J, Jansson T, Persson HW, Lindström
599 K. Longitudinal movements and resulting shear strain of the arterial
600 wall. American Journal of Physiology – Heart and Circulatory Physiol-
601 ogy, 2006;291:H394–H402.
- 602 Cinthio M, Ahlgren ÅR, Jansson T, Eriksson A, Persson H, Lindstrom K.
603 Evaluation of an ultrasonic echo-tracking method for measurements of arte-

- 604 rial wall movements in two dimensions. *IEEE Transactions on Ultrasonics,*
605 *Ferroelectrics, and Frequency Control*, 2005;52:1300–1311.
- 606 Coleman TF, Li Y. An interior trust region approach for nonlinear minimiza-
607 tion subject to bounds. *SIAM Journal on Optimization*, 1996;6:418–445.
- 608 Department of Health Statistics and Information Systems, WHO. WHO
609 methods and data sources for country-level causes of death 2000–2015.
610 Tech. rep., World Health Organization, Geneva, 2016.
- 611 Duda RO, Hart PE. Use of the Hough transformation to detect lines and
612 curves in pictures. *Communications of the ACM*, 1972;15:11–15.
- 613 Duprez DA, Cohn JN. Arterial stiffness as a risk factor for coronary
614 atherosclerosis. *Current Atherosclerosis Reports*, 2007;9:139–144.
- 615 Gastouniotti A, Golemati S, Stoitsis J, Nikita K. Kalman-filter-based block
616 matching for arterial wall motion estimation from B-mode ultrasound. In:
617 *Proc. IEEE International Conference on Imaging Systems and Techniques.*
618 *Thessaloniki, Greece, 2010.* pp. 234–239.
- 619 Gastouniotti A, Tsiaparas NN, Golemati S, Stoitsis JS, Nikita K. Affine op-
620 tical flow combined with multiscale image analysis for motion estimation
621 of the arterial wall from B-mode ultrasound. In: *Proc. 33rd Annual In-*
622 *ternational Conference of the IEEE Engineering in Medicine and Biology*
623 *Society (EMBC). Boston, MA, USA, 2011.* pp. 559–562.
- 624 Golemati S, Sassano A, Lever MJ, Bharath AA, Dhanjil S, Nicolaidis AN.
625 Carotid artery wall motion estimated from B-mode ultrasound using re-

626 gion tracking and block matching. *Ultrasound in Medicine & Biology*,
627 2003;29:387–399.

628 Golemati S, Stoitsis J, Gastounioti A, Dimopoulos A, Koropouli V, Nikita K.
629 Comparison of block matching and differential methods for motion analysis
630 of the carotid artery wall from ultrasound images. *IEEE Transactions on*
631 *Information Technology in Biomedicine*, 2012;16:852–858.

632 Golemati S, Stoitsis J, Sifakis EG, Balkizas T, Nikita KS. Using the
633 Hough transform to segment ultrasound images of longitudinal and trans-
634 verse sections of the carotid artery. *Ultrasound in Medicine & Biology*,
635 2007;33:1918–1932.

636 Gonzalez RC, Woods RE. *Digital Image Processing*, 3rd Edition. Prentice-
637 Hall, Upper Saddle River, NJ, USA, 2006.

638 Gosling RG, Budge MM. Terminology for describing the elastic behavior of
639 arteries. *Hypertension*, 2003;41:1180–1182.

640 Guerrero J, Salcudean S, McEwen J, Masri B, Nicolaou S. Real-time ves-
641 sel segmentation and tracking for ultrasound imaging applications. *IEEE*
642 *Transactions on Medical Imaging*, 2007;26:1079–1090.

643 Harris C, Stephens M. A combined corner and edge detector. In: *Proc. 4th*
644 *Alvey Vision Conference*. Manchester, UK, 1988. pp. 147–151.

645 Horn BKP, Schunck BG. Determining optical flow. *Artificial Intelligence*,
646 1981;17:185–203.

- 647 Jensen JA. Field: A program for simulating ultrasound systems. *Medical &*
648 *Biological Engineering & Computing*, 1997;34:351–353.
- 649 Jensen JA, Munk P. Computer phantoms for simulating ultrasound B-mode
650 and CFM images. In: Lees S, Ferrari LA (Eds.), *Acoustical Imaging*.
651 Vol. 23. Springer, New York, USA, Ch. 12, 1997. pp. 75–80.
- 652 Lindeberg T. Scale-space theory: A basic tool for analysing structures at
653 different scales. *Journal of Applied Statistics*, 1994;21:224–270.
- 654 Liu S, Padfield D, Mendonca P. Tracking of carotid arteries in ultrasound
655 images. In: Proc. 16th International Conference on Medical Image Com-
656 puting and Computer-Assisted Intervention (MICCAI). Nagoya, Japan,
657 2013. pp. 526–533.
- 658 Lowe DG. Object recognition from local scale-invariant features. In: Proc.
659 7th IEEE International Conference on Computer Vision (ICCV '99) – Vol-
660 ume 2. Kerkyra, Greece, 1999. pp. 1150–1157.
- 661 Lucas BD, Kanade T. An iterative image registration technique with an
662 application to stereo vision. In: Proc. 7th International Joint Conference
663 on Artificial Intelligence (IJCAI'81) – Volume 2. Vancouver, Canada, 1981.
664 pp. 674–679.
- 665 Milnor W. *Hemodynamics*. Williams & Wilkins, 1982.
- 666 Rosten E, Drummond T. Machine learning for high-speed corner detection.
667 In: Proc. 9th European Conference on Computer Vision (ECCV'06) – Part
668 I. Graz, Austria, 2006. pp. 430–443.

- 669 Schlaikjer M, Petersen ST, Jensen J, Stetson P. Tissue motion in blood velocity
670 estimation and its simulation. In: Proc. IEEE Ultrasonics Symposium.
671 Vol. 2. Sendai, Japan, 1998. pp. 1495–1499.
- 672 Shi J, Tomasi C. Good features to track. In: Proc. IEEE Computer Society
673 Conference on Computer Vision and Pattern Recognition (CVPR '94).
674 Seattle, WA, USA, 1994. pp. 593–600.
- 675 Stoitsis J, Golemati S, Bastouni E, Nikita K. A mathematical model of the
676 mechanical deformation of the carotid artery wall and its application to
677 clinical data. In: Proc. 29th Annual International Conference of the IEEE
678 Engineering in Medicine and Biology Society (EMBS'07). Lyon, France,
679 2007. pp. 2163–2166.
- 680 Stoitsis J, Golemati S, Koropouli V, Nikita K. Simulating dynamic B-mode
681 ultrasound image data of the common carotid artery. In: Proc. IEEE Inter-
682 national Workshop on Imaging Systems and Techniques (IST'08). Chania,
683 Greece, 2008. pp. 144–148.
- 684 Tat J, Au JS, Keir PJ, MacDonald MJ. Reduced common carotid artery
685 longitudinal wall motion and intramural shear strain in individuals with
686 elevated cardiovascular disease risk using speckle tracking. *Clinical Physi-
687 ology and Functional Imaging* (2015), 2015.
- 688 Thangavel M, Chandrasekaran M, Madheswaran M. Wall motion analysis
689 of common carotid artery and detection of abnormality using transverse
690 ultrasound images. *Research Journal of Applied Sciences, Engineering and
691 Technology*, 2014;7:1076–1082.

- 692 Viola P, Jones M. Robust real-time object detection. *International Journal*
693 *of Computer Vision*, 2001;57:137–154.
- 694 Říha K, Beneš R. Circle detection in pulsative medical video sequence. In:
695 *Proc. 10th IEEE International Conference on Signal Processing (ICSP)*.
696 Beijing, China, 2010. pp. 674–677.
- 697 Říha K, Mašek J, Burget R, Beneš R, Závodná E. Novel method for local-
698 ization of common carotid artery transverse section in ultrasound images
699 using modified Viola-Jones detector. *Ultrasound in Medicine & Biology*,
700 2013;39:1887–1902.
- 701 Říha K, Potůček I. The sequential detection of artery sectional area using
702 optical flow technique. In: *Proc. 8th WSEAS International Conference on*
703 *Circuits, Systems, Electronics, Control & Signal Processing (CSECS'09)*.
704 Puerto De La Cruz, Tenerife, Spain, 2009. pp. 222–226.
- 705 Wang D, Klatzky R, Wu B, Weller G, Sampson A, Stetten G. Fully au-
706 tomated common carotid artery and internal jugular vein identification
707 and tracking using B-mode ultrasound. *IEEE Transactions on Biomedical*
708 *Engineering*, 2009;56:1691–1699.
- 709 Zahnd G, Orkisz M, Sérusclat A, Moulin P, Vray D. Evaluation of a Kalman-
710 based block matching method to assess the bi-dimensional motion of the
711 carotid artery wall in B-mode ultrasound sequences. *Medical Image Anal-*
712 *ysis*, 2013;17:573–585.

Figure Captions

Figure 1: Flowchart of the proposed method.

Figure 2: Example of the result of artery detection using the modified Viola-Jones detector. The figure shows the recorded US image and a white square indicating the region of interest determined by the detector.

Figure 3: Example of the ten first (highest-confidence) circles produced by the Hough transform.

Figure 4: Annular search region for IP detection.

Figure 5: Example of detected IPs (represented by white circles).

Figure 6: Example of the feature drift effect: (a) Initial set of IPs, (b) IPs at a later frame time without feature drift compensation.

Figure 7: Example of IP tracking. Circles represent IPs (after moving), crosses represent removed IPs, and squares represent added IPs.

Figure 8: Estimated AWC radius function extracted by the reference method from a real US video sequence: (a) Estimated radius function $\hat{r}_{\text{ref}}(t)$ spanning approximately 30 cardiac cycles, (b) normalized one-cycle displacement function $\hat{d}_{\text{ref}}(t)$.

Figure 9: Simulated (fitted) AWC radius function obtained using the radial part of the motion model described in [Stoitsis et al. \(2008\)](#): (a) Normalized one-cycle displacement function $d(t)$, (b) radius function $r_0(t)$

spanning approximately 22 cardiac cycles and including breathing artifacts.

Figure 10: Measured US image underlying the “uncorrupted” sequence S_0 .

Figure 11: Four frames from the sequence with global movement S_P .

Figure 12: Example images from the sequences S_{S25} (left) and S_{S15} (right) containing speckle noise with an SNR of 25 dB and 15 dB, respectively.

Figure 13: Example images from the sequences S_{G25} (left) and S_{G15} (right) containing additive Gaussian noise with an SNR before clipping of 25 dB and 15 dB, respectively.

Figure 14: Intensity (echogenicity) map. Brighter areas represent more echogenic tissue, i.e., areas with higher scatterer amplitudes.

Figure 15: Simulated image produced by the Field II simulation program and based on the intensity map in Fig. 14.

Figure 16: AWC radius function estimated by the proposed method from real clinical data: (a) healthy 32-year-old subject, (b) 72-year-old subject with atherosclerosis.

Tables

Table 1: RMSE results for the “uncorrupted” sequence S_0 .

IP detector	RMSE [px]	
	Proposed method	Reference method
FAST	0.96	0.53
GFTT	0.46	0.49
Harris	0.77	0.47
Pyr-FAST	0.67	0.55
Pyr-GFTT	0.46	0.49
Pyr-Harris	0.54	0.47
SIFT	3.62	0.48
SURF	4.94	0.84

Table 2: RMSE results for the sequence with global movement S_P .

RMSE [px]		
IP detector	Proposed method	Reference method
FAST	4.06	96.49
GFTT	4.25	23.91
Harris	3.93	42.64
Pyr-FAST	4.50	24.10
Pyr-GFTT	3.54	23.91
Pyr-Harris	3.83	24.03
SIFT	6.36	26.07
SURF	4.88	24.31

Table 3: RMSE results for the sequences with speckle noise S_{S25} and S_{S15} .

IP detector	RMSE [px]			
	Sequence S_{S25}		Sequence S_{S15}	
	Proposed method	Reference method	Proposed method	Reference method
FAST	1.31	2.07	71.08	27.72
GFTT	0.53	2.08	1.85	111.57
Harris	0.52	0.87	2.92	138.69
Pyr-FAST	0.65	1.76	1.37	57.01
Pyr-GFTT	0.95	1.67	3.79	111.57
Pyr-Harris	0.55	0.87	6.75	79.91
SIFT	3.04	1.50	2.75	36.23
SURF	2.98	1.43	3.41	119.24

Table 4: RMSE results for the sequences with additive Gaussian noise S_{G25} and S_{G15} .

IP detector	RMSE [px]			
	Sequence S_{G25}		Sequence S_{G15}	
	Proposed method	Reference method	Proposed method	Reference method
FAST	0.73	0.46	130.75	87.45
GFTT	0.50	0.45	3.51	2.36
Harris	0.55	0.45	2.77	2.64
Pyr-FAST	0.74	0.44	7.23	317.14
Pyr-GFTT	1.85	0.45	3.73	3.10
Pyr-Harris	0.85	0.45	3.68	2.64
SIFT	2.52	0.64	2.50	3.41
SURF	7.93	0.73	7.38	5.81

Table 5: RMSE results for the sequences with simulated feature drift S_{F_2} and S_{F_5} .

IP detector	RMSE [px]			
	Sequence S_{F_2}		Sequence S_{F_5}	
	Proposed method	Reference method	Proposed method	Reference method
FAST	3.41	2.24	2.69	8.54
GFTT	3.49	3.00	1.83	8.29
Harris	2.66	3.13	2.13	10.85
Pyr-FAST	3.46	2.84	3.05	8.45
Pyr-GFTT	3.76	3.00	3.08	8.29
Pyr-Harris	2.85	3.26	2.16	10.85
SIFT	7.71	2.86	3.73	8.92
SURF	5.05	3.45	3.76	6.67

Table 6: Total RMSE for all test sequences.

IP detector	RMSE [px]	
	Proposed method	Reference method
Harris	2.16 ± 1.18	23.56 ± 42.61
GFTT	2.19 ± 1.40	17.43 ± 33.99
Pyr-Harris	2.60 ± 1.88	14.96 ± 24.11
Pyr-GFTT	2.70 ± 1.21	17.46 ± 33.97
Pyr-FAST	2.92 ± 2.15	46.32 ± 97.30
SIFT	3.88 ± 1.77	9.30 ± 12.15
SURF	4.77 ± 1.76	18.58 ± 36.24
FAST	24.69 ± 43.12	25.58 ± 36.43

Table 7: Runtimes of artery region/parameter estimation, IP tracking, and feature drift compensation for the test sequences with image resolution 370×370 px.

Sequence	Runtime [ms]					
	S_0	S_P	S_{S25}	S_{S15}	S_{G25}	S_{G15}
Algor. part						
Artery region/ parameter est.	32.2 ± 5.6	27.7 ± 10.4	36.7 ± 6.8	49.2 ± 11.5	33.8 ± 7.6	69.6 ± 17.4
IP tracking	1.2 ± 0.2	1.2 ± 0.2	1.2 ± 0.1	1.3 ± 0.1	1.2 ± 0.0	1.3 ± 0.1
Feature drift compens.	2.0 ± 0.5	1.9 ± 0.5	1.9 ± 0.4	1.9 ± 0.4	1.8 ± 0.4	1.9 ± 1.2

Table 8: Runtime of IP detection for the test sequences with image resolution 370×370 px.

Sequence	Runtime [ms]					
	S_0	S_P	S_{S25}	S_{S15}	S_{G25}	S_{G15}
IP detector						
FAST	0.8 ± 0.3	0.8 ± 0.3	0.8 ± 0.1	1.0 ± 0.0	0.7 ± 0.0	2.4 ± 0.1
GFTT	3.9 ± 0.0	4.0 ± 0.1	4.0 ± 0.1	4.0 ± 0.1	4.0 ± 0.1	3.9 ± 0.1
Harris	3.8 ± 0.0	3.9 ± 0.0	3.9 ± 0.0	3.9 ± 0.1	3.8 ± 0.0	4.1 ± 0.0
Pyr-FAST	1.9 ± 0.1	1.9 ± 0.0	2.0 ± 0.0	2.3 ± 0.1	2.0 ± 0.0	3.8 ± 22.3
Pyr-GFTT	7.9 ± 0.1	7.9 ± 0.2	7.9 ± 0.1	8.0 ± 0.1	7.9 ± 0.2	7.9 ± 0.0
Pyr-Harris	7.8 ± 0.1	8.1 ± 0.1				
SIFT	50.5 ± 0.9	50.8 ± 0.5	51.6 ± 0.5	51.8 ± 0.5	48.3 ± 0.5	56.5 ± 0.0
SURF	4.9 ± 0.0	4.9 ± 0.0	4.9 ± 0.0	5.0 ± 0.1	5.2 ± 0.0	5.2 ± 0.1

Table 9: Runtimes of artery region/parameter estimation, IP tracking, and feature drift compensation for the test sequences with image resolution 490×490 px.

Sequence	Runtime [ms]		
	S_{F0}	S_{F2}	S_{F5}
Algorithm part			
Artery region/parameter estimation	68.5 ± 3.2	64.1 ± 4.8	45.3 ± 4.6
IP tracking	2.0 ± 0.1	2.0 ± 0.1	2.0 ± 0.1
Feature drift compensation	2.9 ± 0.4	3.1 ± 0.5	3.0 ± 0.4

Table 10: Runtime of IP detection for the test sequences with image resolution 490×490 px.

Sequence	Runtime [ms]		
	S_{F0}	S_{F2}	S_{F5}
IP detector			
FAST	2.1 ± 0.1	1.9 ± 0.1	1.7 ± 0.1
GFTT	7.0 ± 0.1	7.0 ± 0.1	6.9 ± 0.1
Harris	6.8 ± 0.1	6.8 ± 0.1	6.7 ± 0.1
Pyr-FAST	4.7 ± 0.1	4.5 ± 0.1	4.2 ± 0.2
Pyr-GFTT	14.1 ± 0.1	14.0 ± 0.1	14.0 ± 0.1
Pyr-Harris	13.7 ± 0.2	13.8 ± 0.1	13.9 ± 0.1
SIFT	87.9 ± 0.7	85.9 ± 0.6	85.8 ± 0.7
SURF	9.3 ± 0.1	9.2 ± 0.1	9.0 ± 0.2

Figure_01
Click here to download Figure: figure_01.pdf

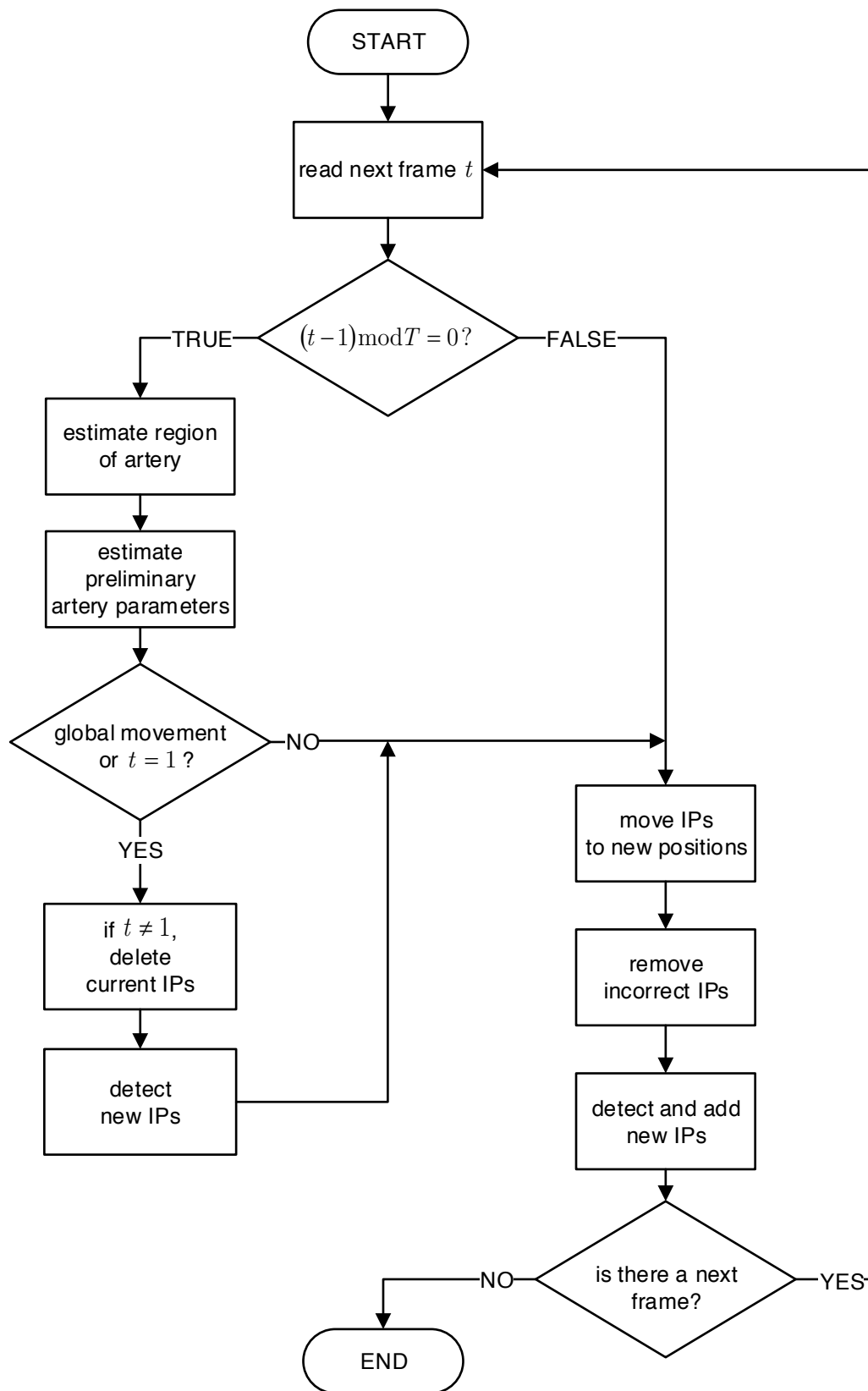


Figure_02
[Click here to download high resolution image](#)



Figure_03
[Click here to download high resolution image](#)



Figure_04

[Click here to download Figure: figure_04.pdf](#)

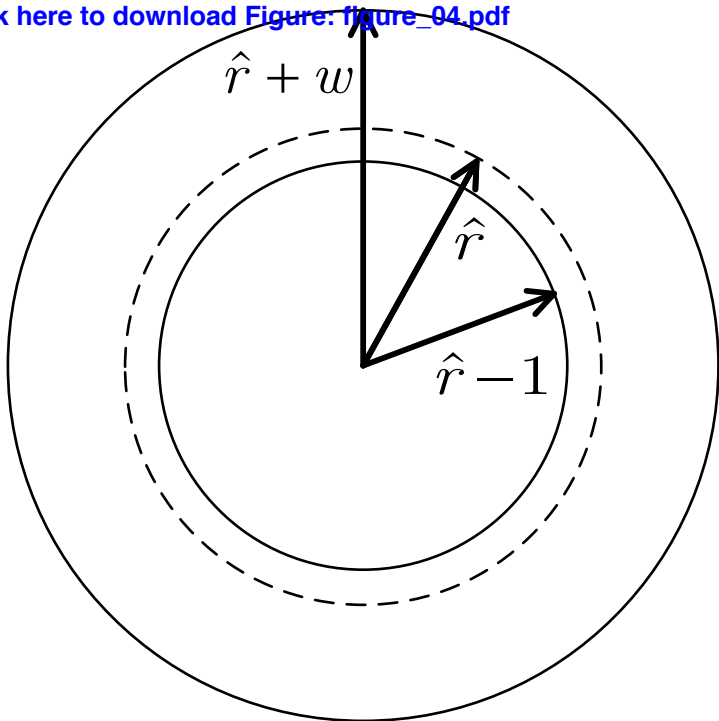


Figure_05
[Click here to download high resolution image](#)

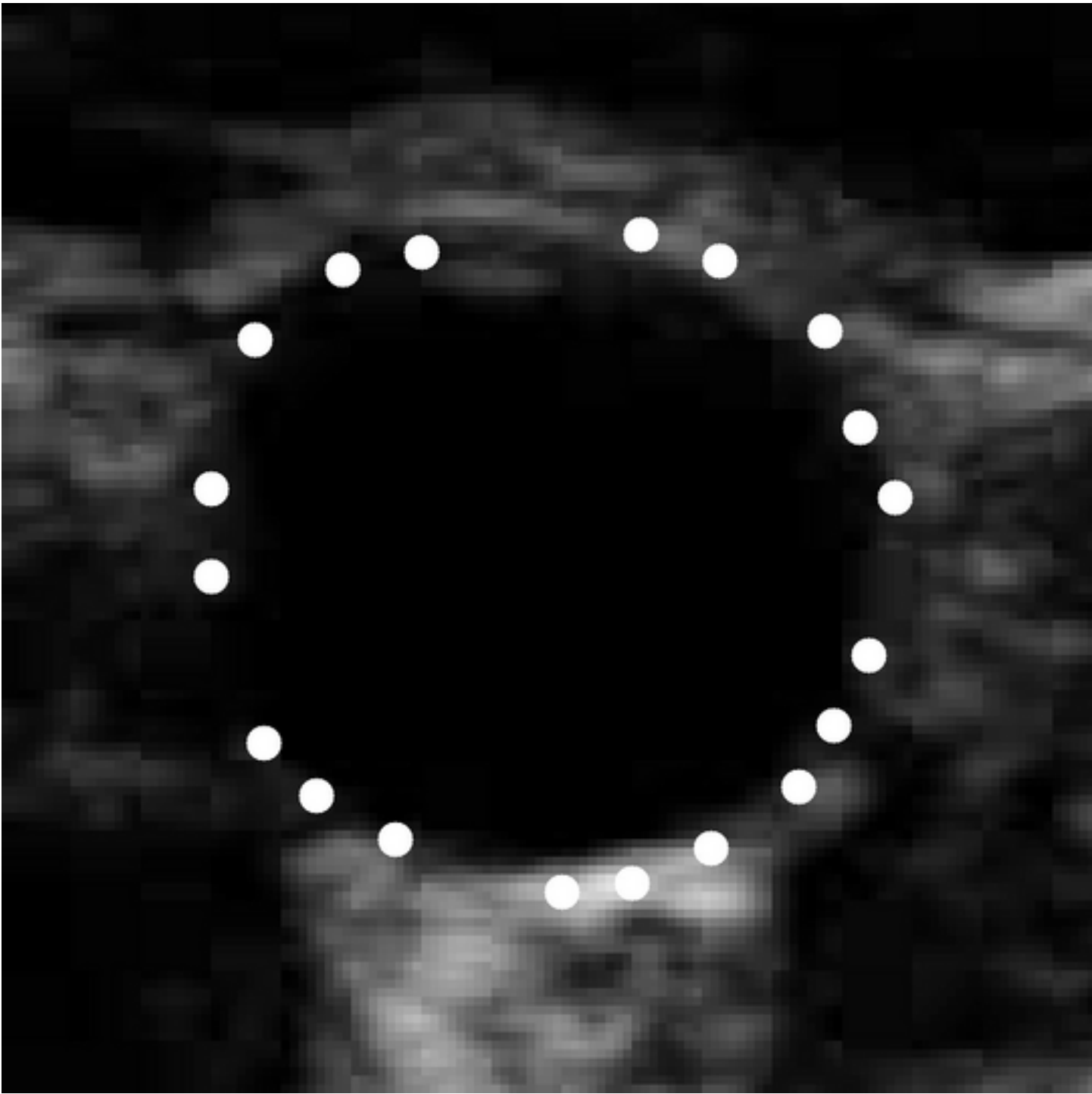


Figure_06_a
[Click here to download high resolution image](#)

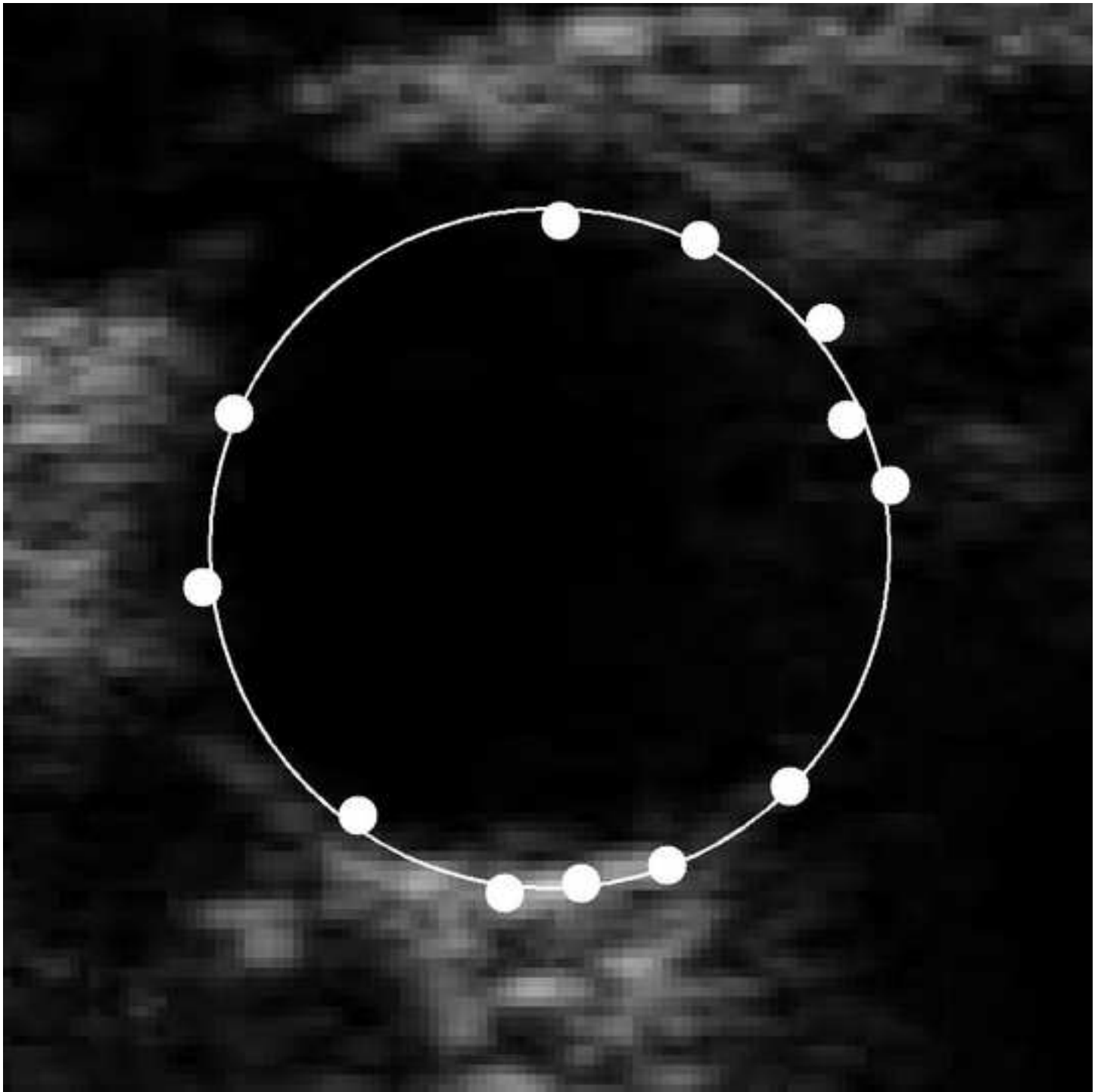


Figure_06_b
[Click here to download high resolution image](#)

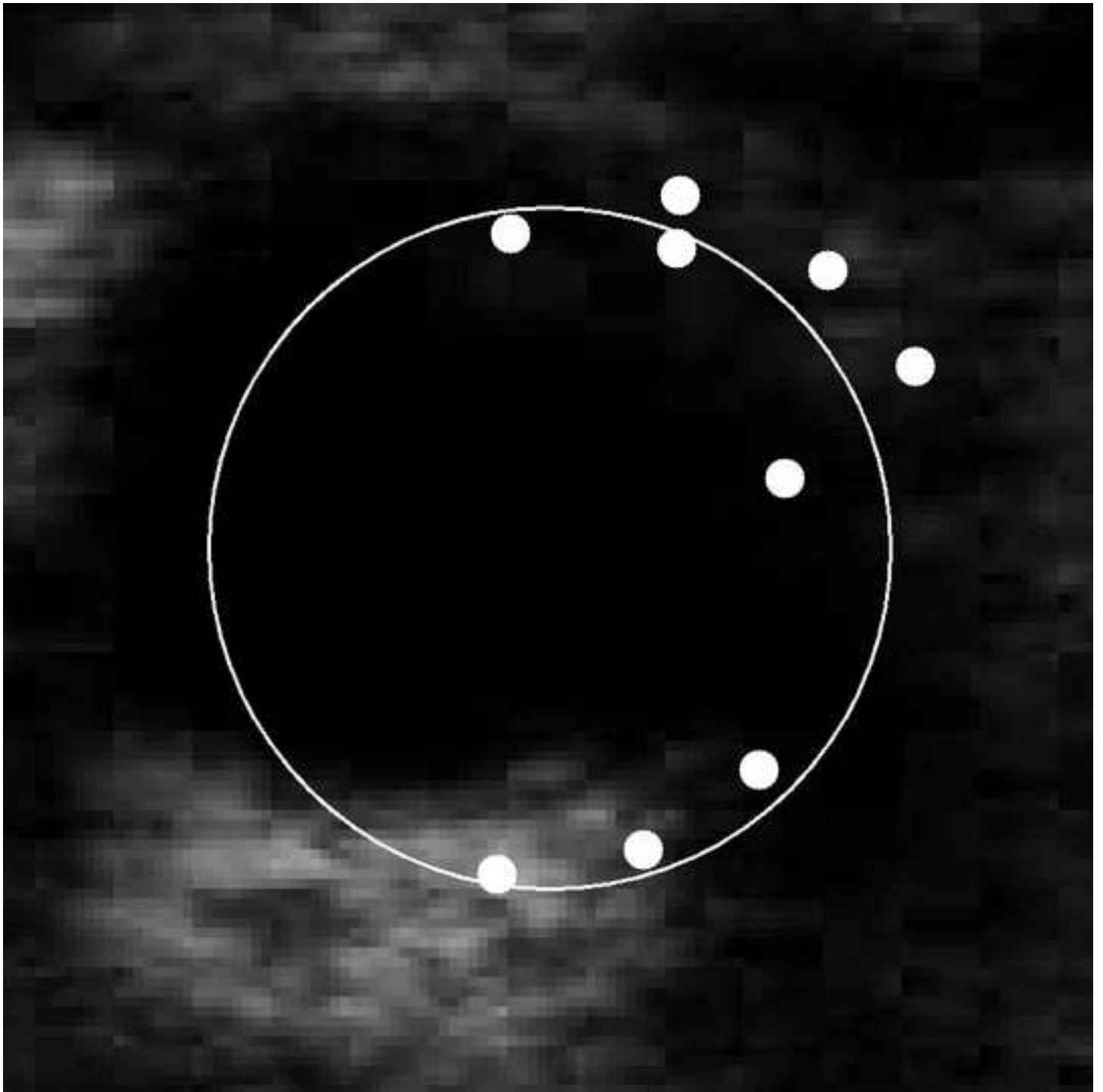


Figure_07
[Click here to download high resolution image](#)

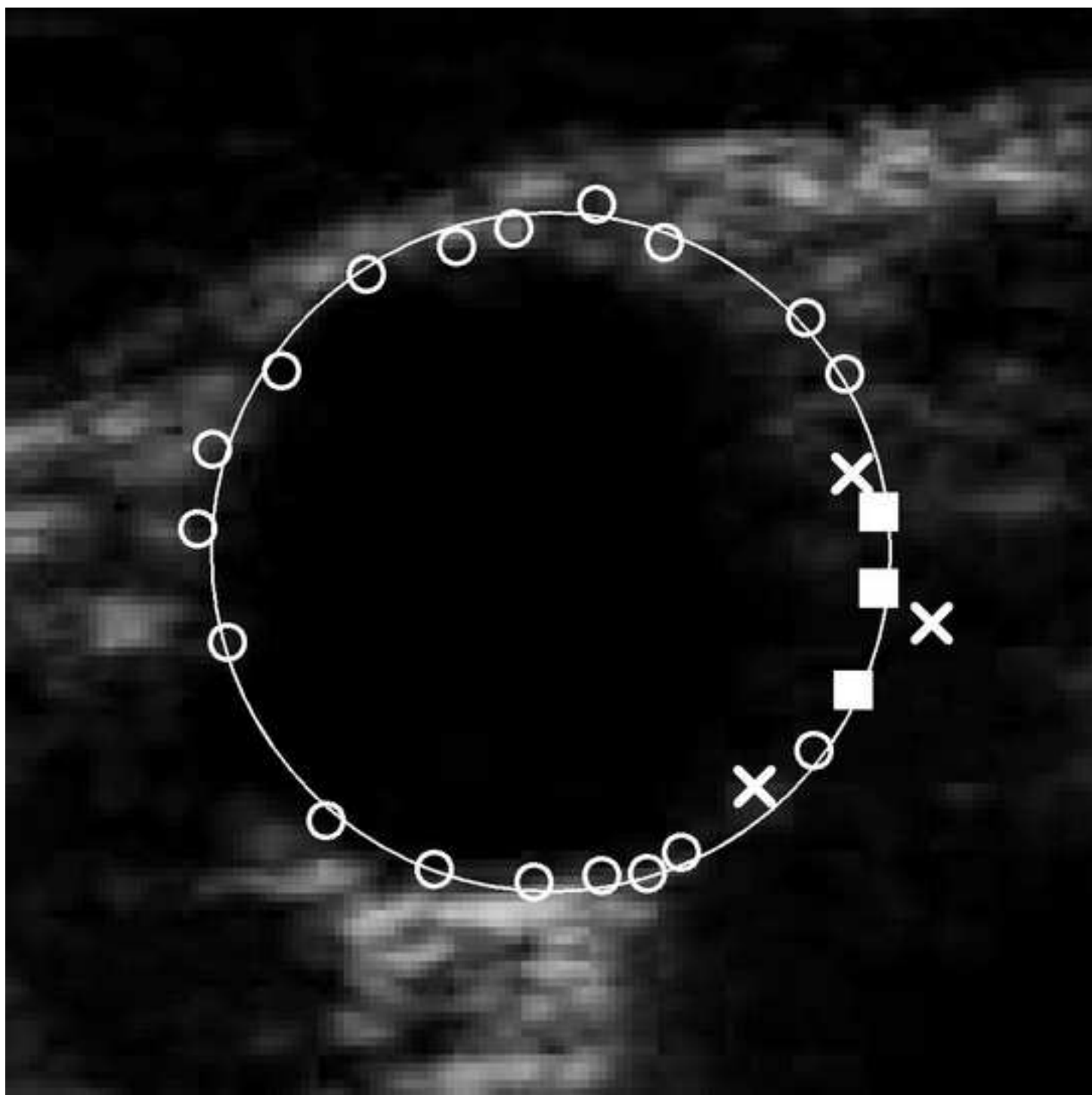


Figure_08_a
[Click here to download Figure: figure_08_a.pdf](#)

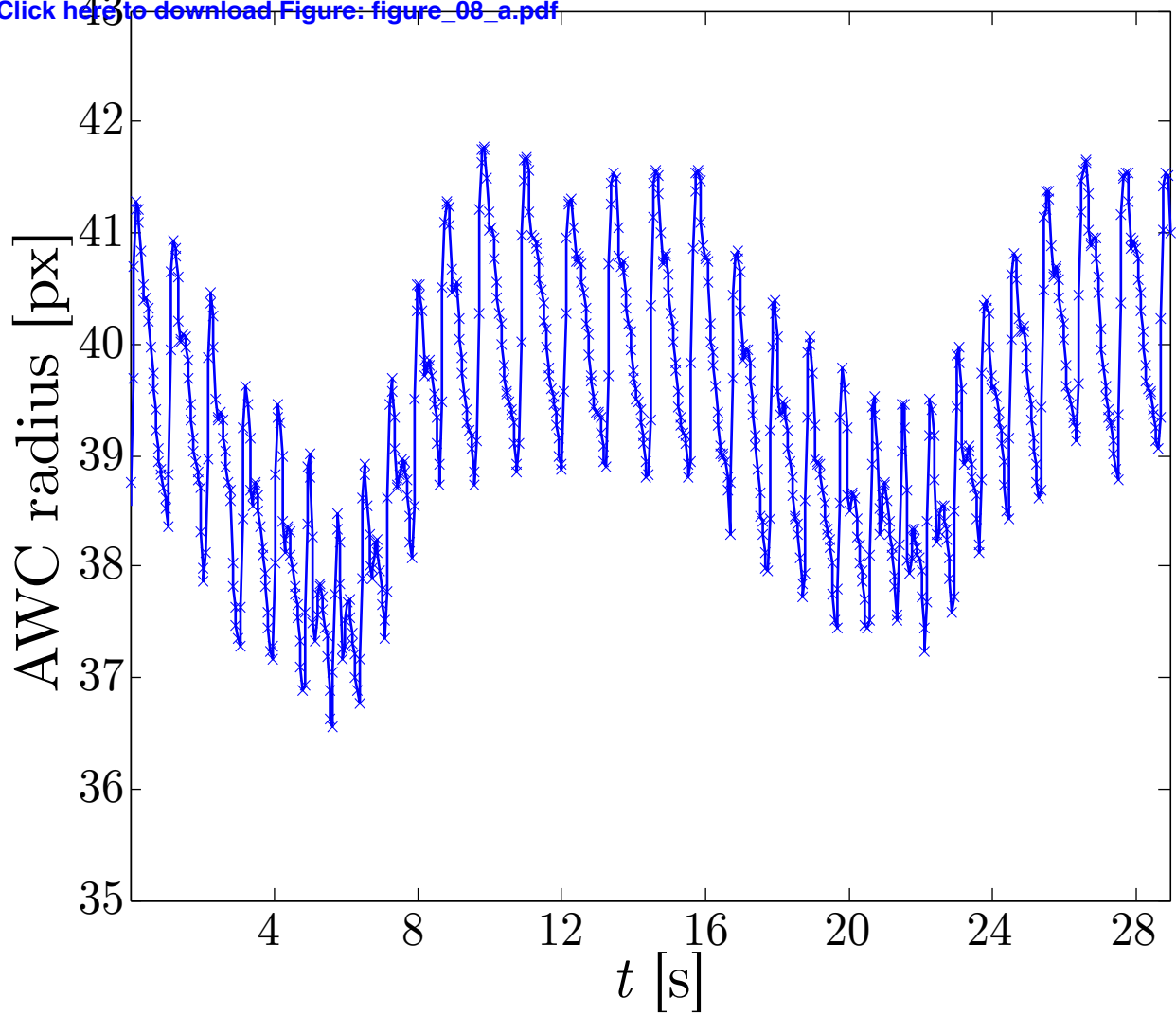


Figure_08_b

[Click here to download Figure: figure_08_b.pdf](#)

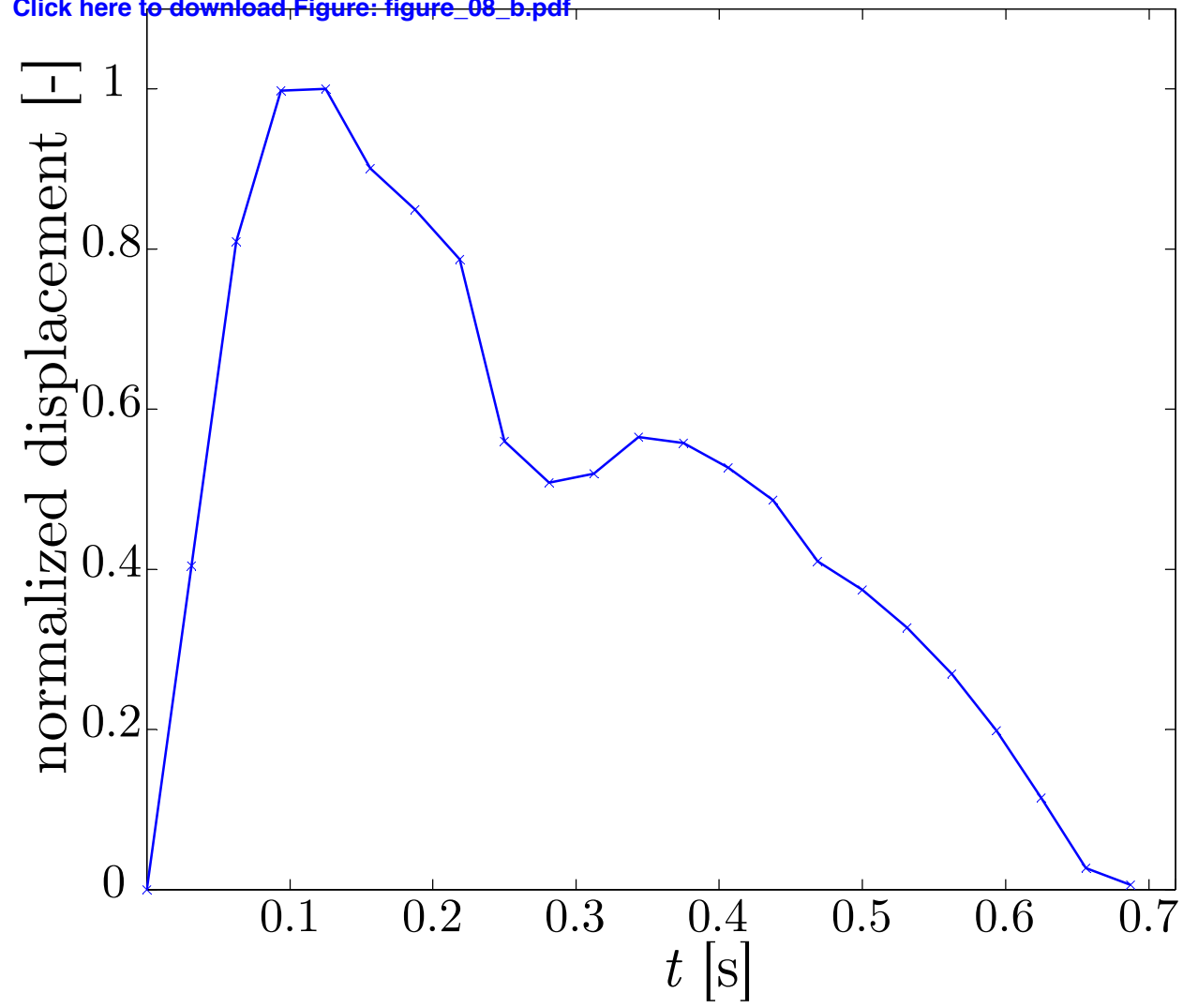


Figure_09_a

[Click here to download Figure: figure_09_a.pdf](#)

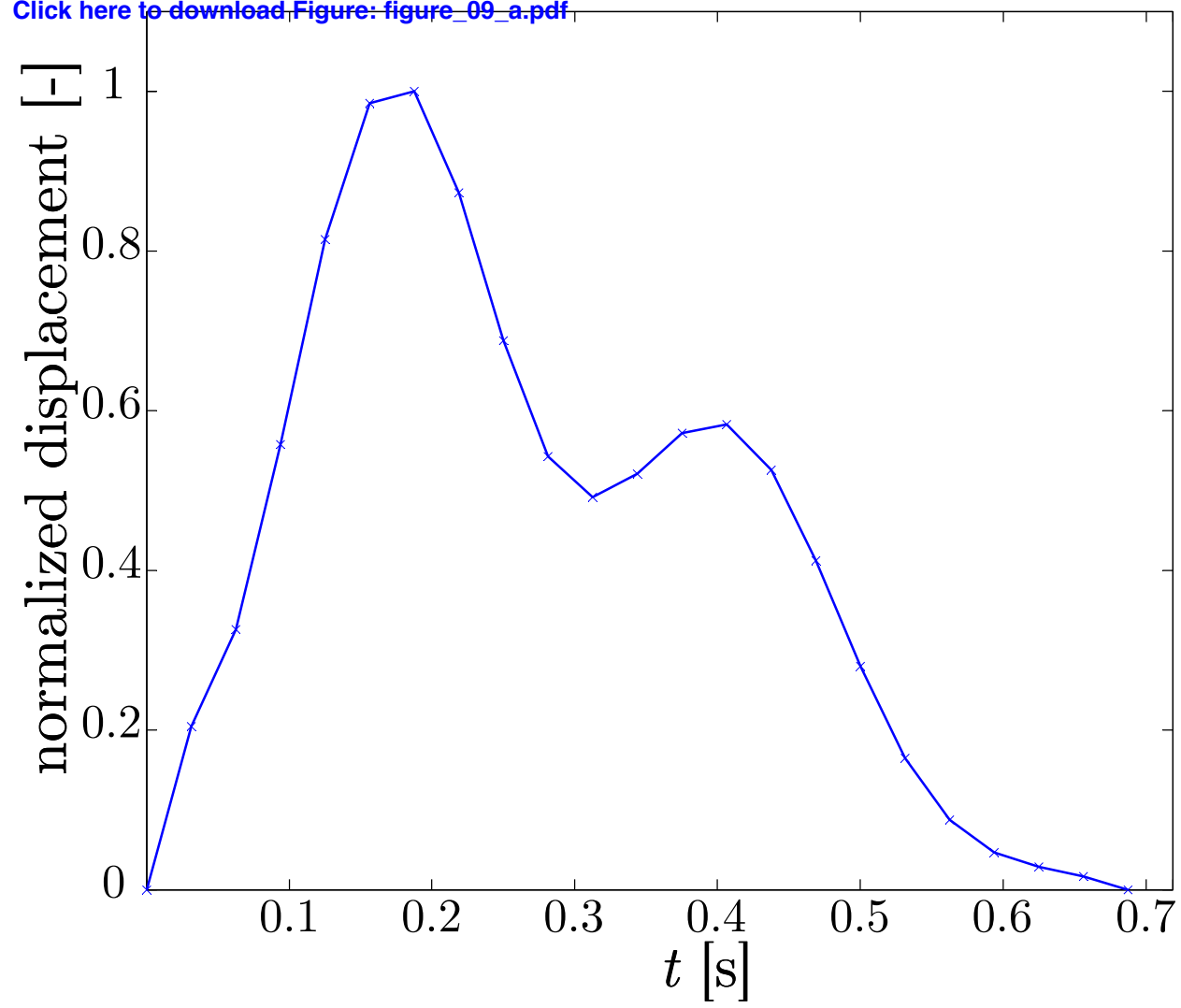


Figure_09_b
[Click here to download Figure: figure_09_b.pdf](#)

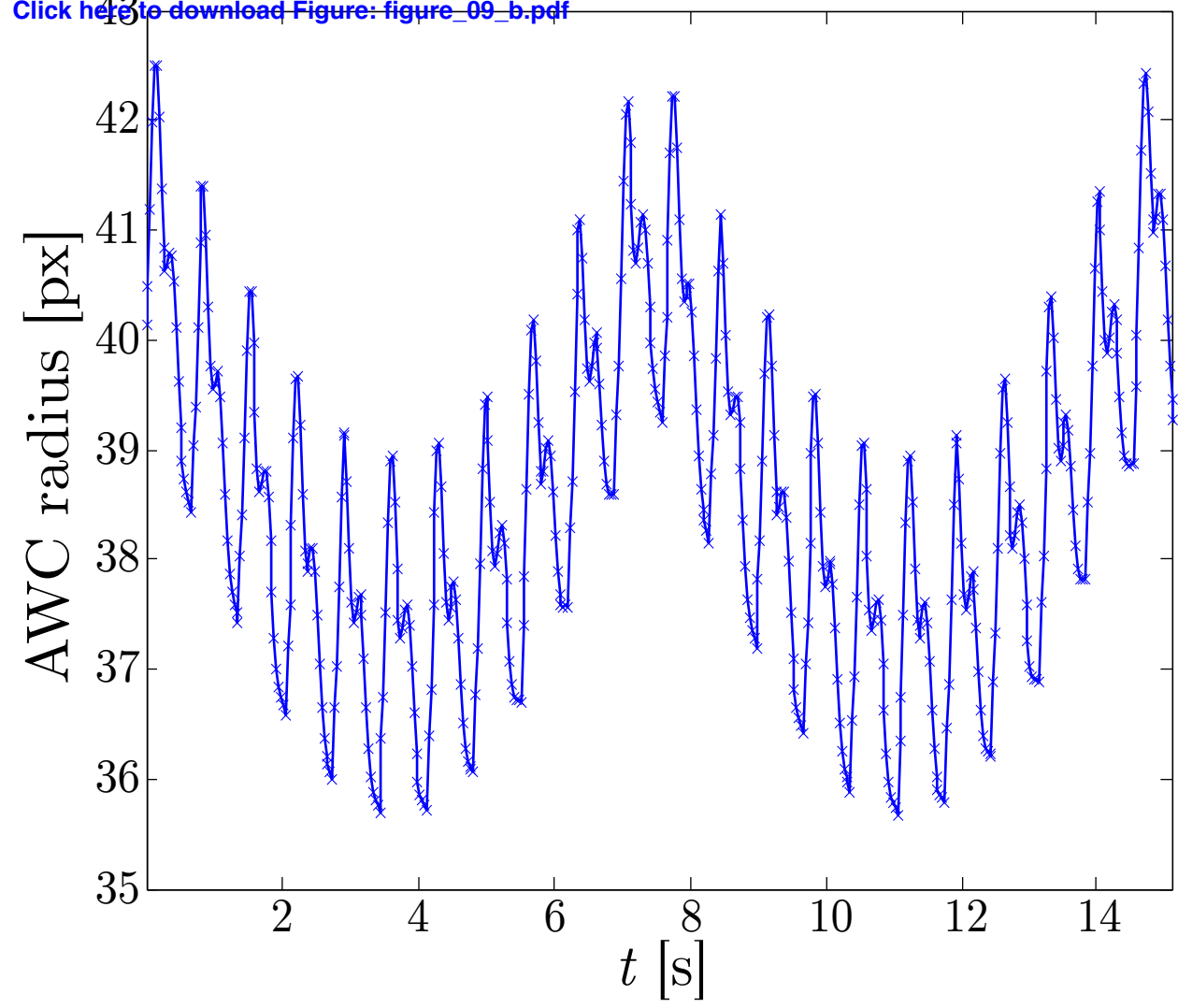


Figure_10
[Click here to download high resolution image](#)



Figure_11_frame663

[Click here to download high resolution image](#)



Figure_11_frame671
[Click here to download high resolution image](#)

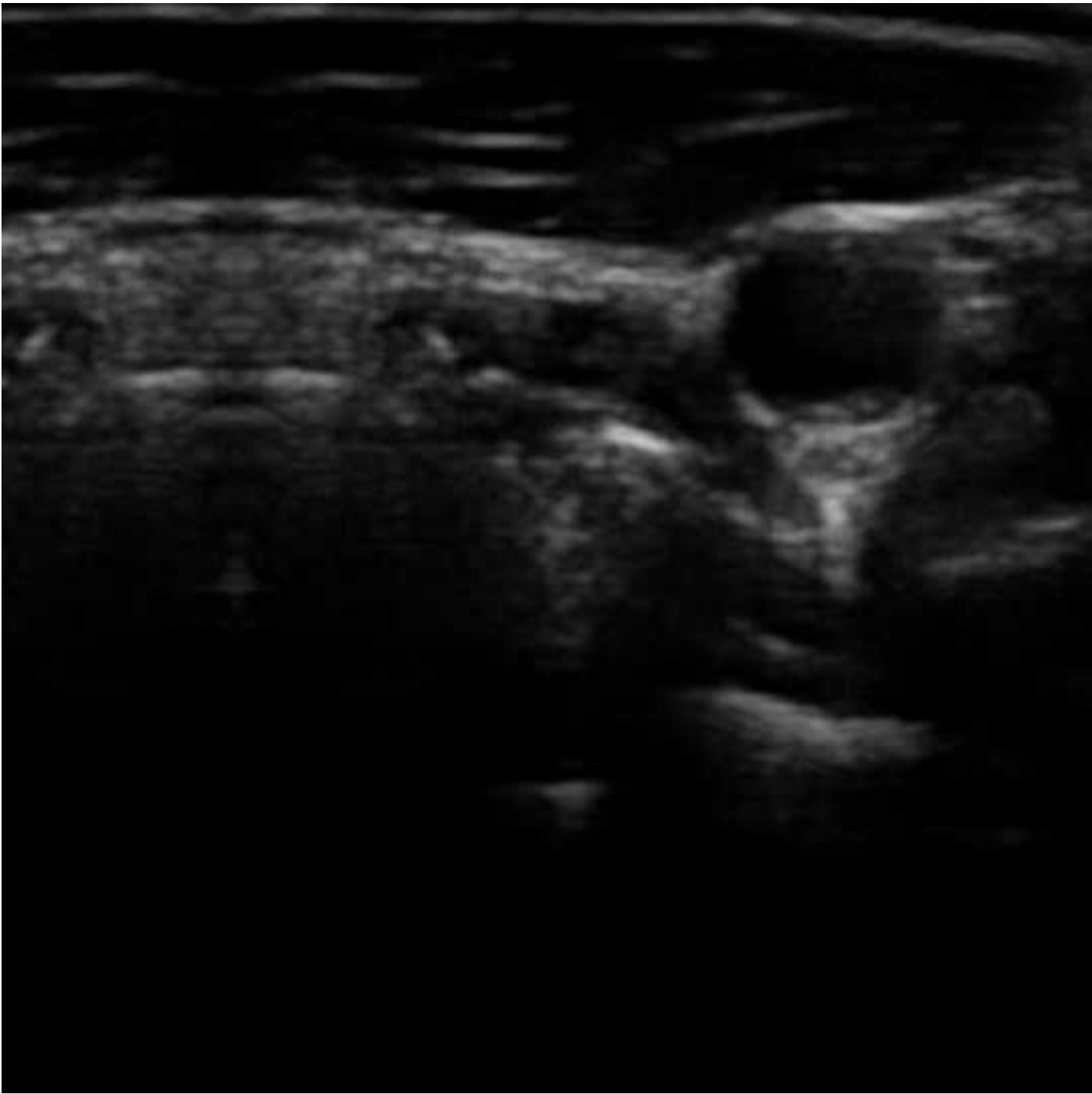


Figure_11_frame679

[Click here to download high resolution image](#)

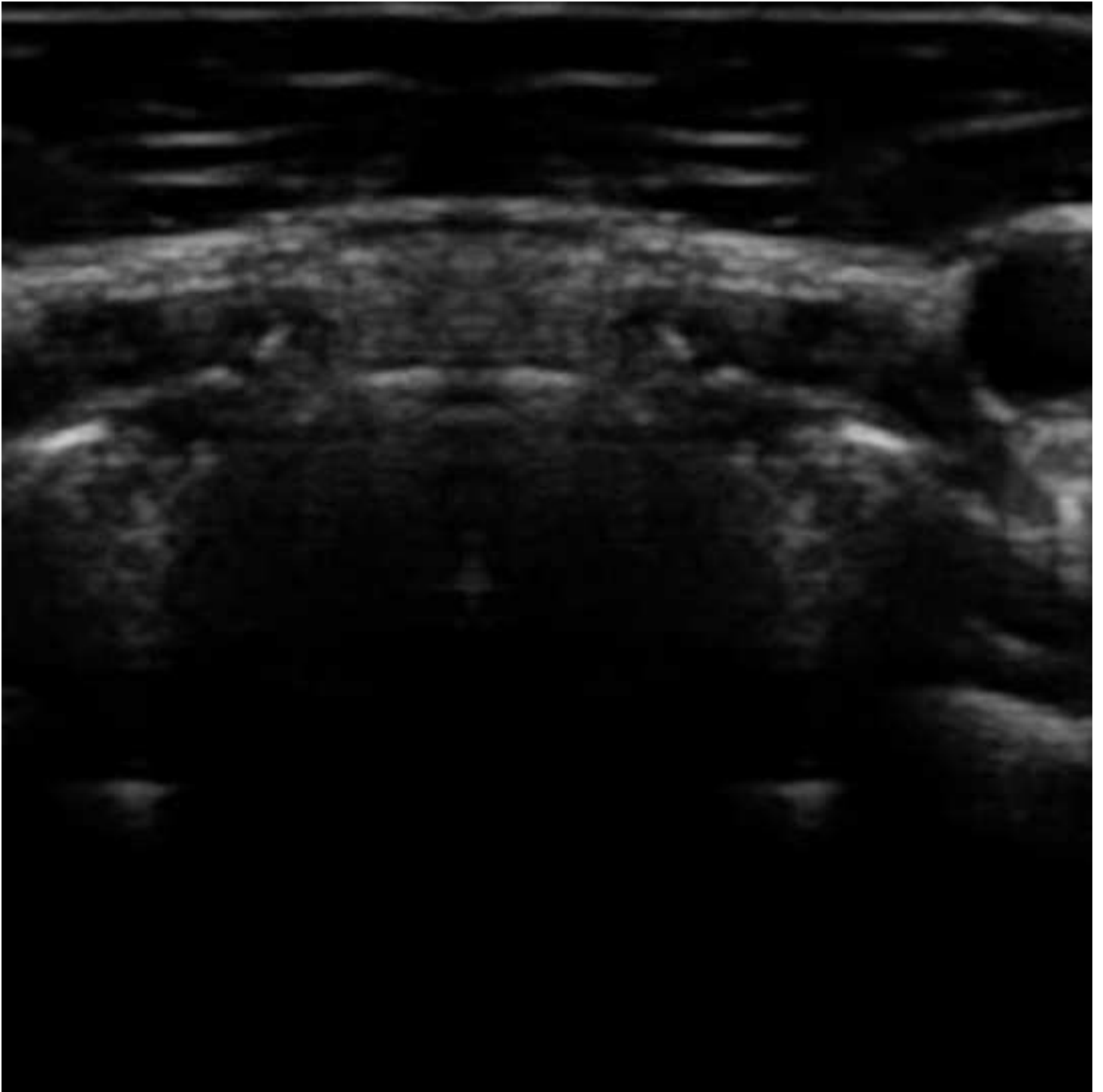


Figure_11_frame687

[Click here to download high resolution image](#)

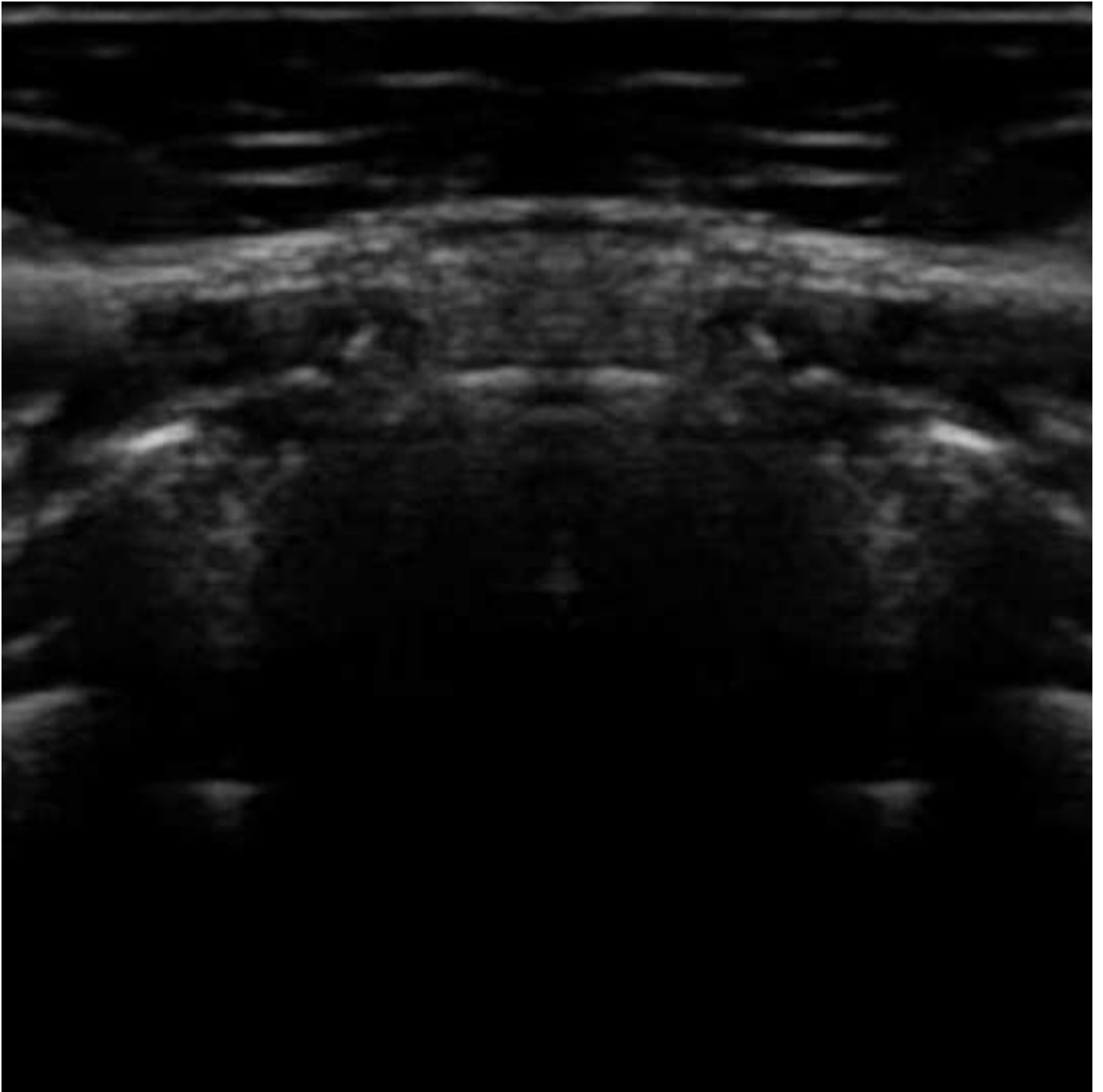


Figure_12_15dB

[Click here to download high resolution image](#)



Figure_12_25dB
[Click here to download high resolution image](#)



Figure_13_15dB
[Click here to download high resolution image](#)



Figure_13_25dB
[Click here to download high resolution image](#)



Figure_14
[Click here to download high resolution image](#)

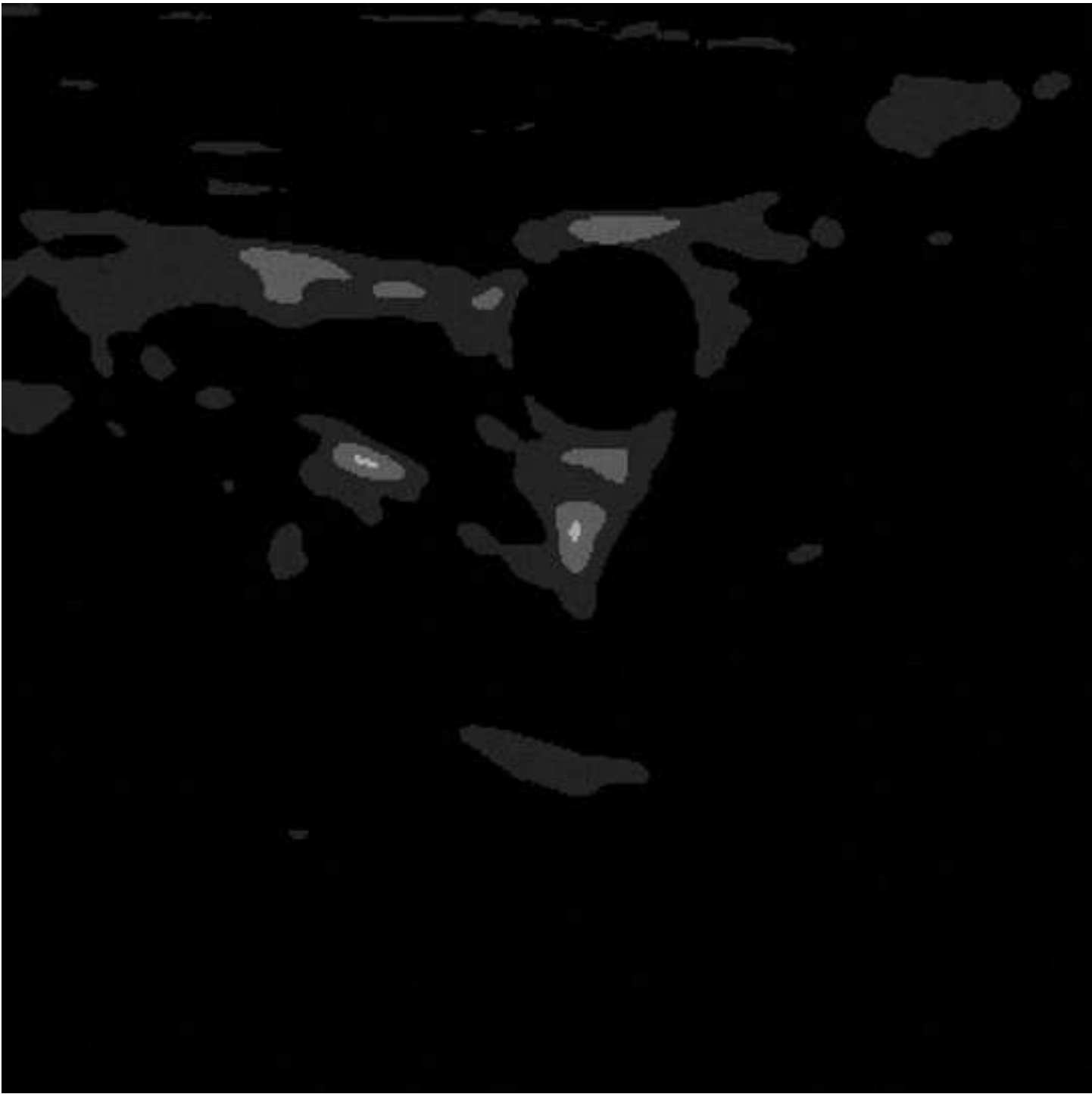
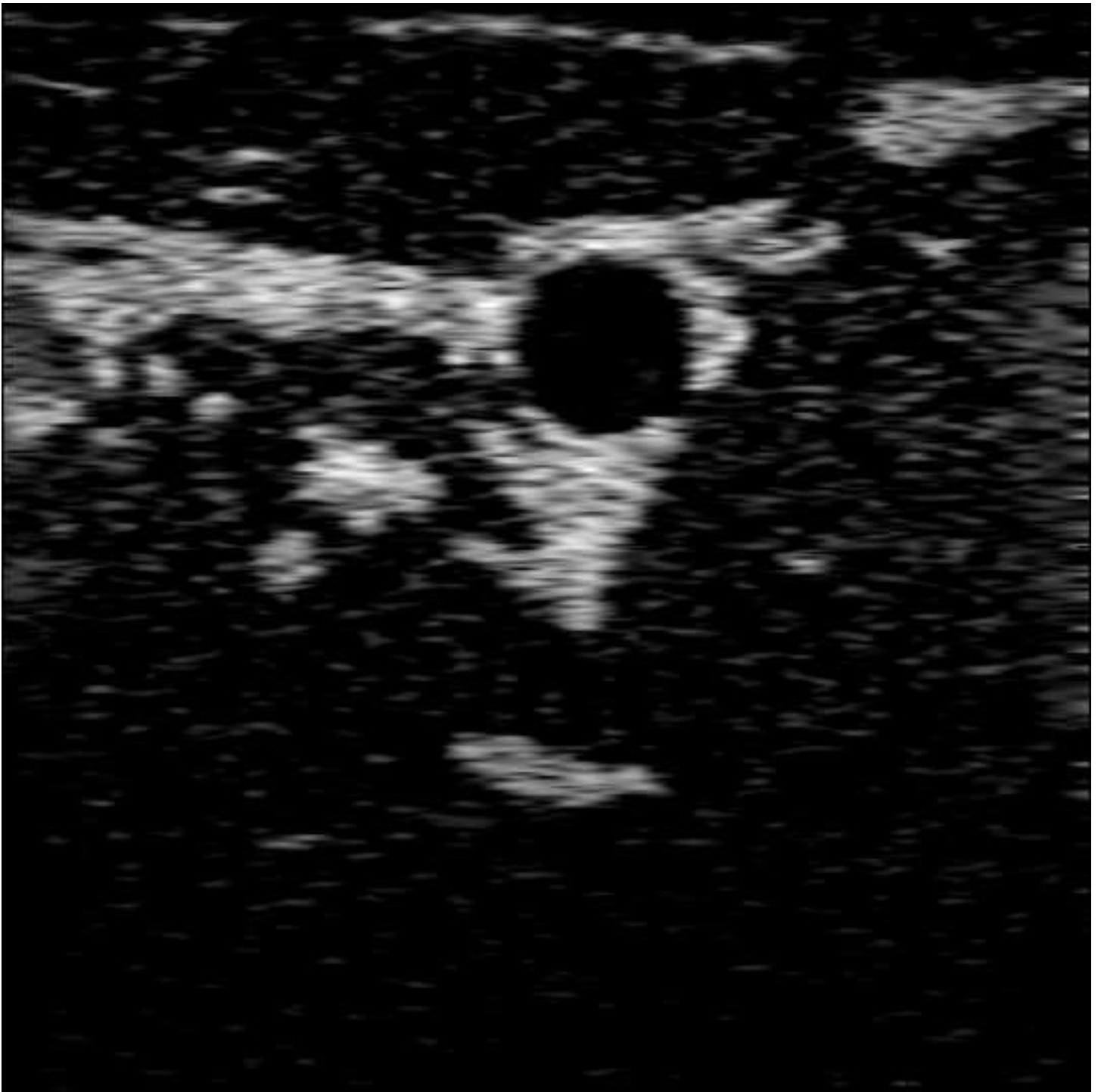


Figure_15
[Click here to download high resolution image](#)



LaTeX Source Files

[Click here to download LaTeX Source Files: tex_files.zip](#)